CZECH TECHNICAL UNIVERSITY IN PRAGUE
FACULTY OF CIVIL ENGINEERING
Department of Mechanics

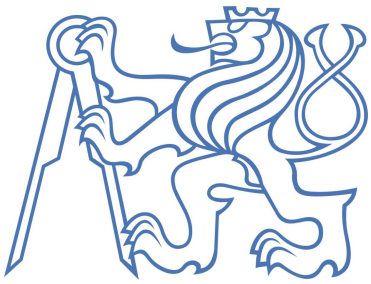

DIPLOMA THESIS

Numerical Simulation of Cocciopesto-based Masonry Structures

Michael Somr

2011

Supervisor: Jan Zeman

Honesty Declaration

I declare that this diploma thesis has been carried out by me and only with the use of materials that are stated in the literature sources.

Prague, 7 December 2011 Michael Somr

.....

Acknowledgement

First of all, I would like to thank my supervisor Jan Zeman, who trusted me, believed in me and my abilities, and spent many hours of his precious time explaining me whatever I needed. I also thank Professor Petr Kabele, who provided me with a lot of valuable information and computer, for the opportunity to work as a member of his team.

Special thanks go to my parents Petra and Dušan for their love and continuous support, to my friend Václav Nežerka for his advice and willingness to discuss any problem I encountered, and to my sister Martina and girlfriend Pája for their tolerance, patience and help with an aesthetic part of my thesis.

Finally, I would like to thank for the financial support by the grant no. DF11P01OVV008.

ČESKÉ VYSOKÉ UČENÍ TECHNICKÉ V PRAZE
Fakulta stavební
Thákurova 7, 166 29 Praha 6

ZADÁNÍ DIPLOMOVÉ PRÁCE

studijní program: Civil Engineering
studijní obor: Building Structures
akademický rok: 2011/2012

Jméno a příjmení diplomanta: Michael Somr

Zadávající katedra: K132 - Katedra mechaniky

Vedoucí diplomové práce: Doc. Ing. Jan Zeman, Ph.D.

Název diplomové práce: Numerical simulation of cocciopesto-based masonry structures
Název diplomové práce v anglickém jazyce: Numerical simulation of cocciopesto-based masonry structures

Rámcový obsah diplomové práce: Studium literatury (chování malty cocciopesto, numerické modelování kvazikřehkých materiálů)

Počítačová simulace experimentu uvedeného v (Binda et. al, Construction and Building Materials, 11 (1), 1997) v systému ATENA (R), zpětná identifikace parametrů modelu

Simulace zděné konstrukce, parametrická studie a určení kritických parametrů modelu

Datum zadání diplomové práce: 14.9.2011 Termín odevzdání: 16.12.2011
(vyplňte poslední den výuky přísl. semestru)

Diplomovou práci lze zapsat, kromě oboru A, v letním i zimním semestru.

Pokud student neodevzdal diplomovou práci v určeném termínu, tuto skutečnost předem písemně zdůvodnil a omluva byla děkanem uznána, stanoví děkan studentovi náhradní termín odevzdání diplomové práce. Pokud se však student řádně neomluvil nebo omluva nebyla děkanem uznána, může si student zapsat diplomovou práci podruhé. Studentovi, který při opakovaném zápisu diplomovou práci neodevzdal v určeném termínu a tuto skutečnost řádně neomluvil nebo omluva nebyla děkanem uznána, se ukončuje studium podle § 56 zákona o VŠ č.111/1998 (SZŘ ČVUT čl 21, odst. 4).

Diplomant bere na vědomí, že je povinen vypracovat diplomovou práci samostatně, bez cizí pomoci, s výjimkou poskytnutých konzultací. Seznam použité literatury, jiných pramenů a jmen konzultantů je třeba uvést v diplomové práci.

Jan Zeman
.....
vedoucí diplomové práce

.....
vedoucí katedry

Zadání diplomové práce převzal dne: 14. 9. 2011

.....
diplomant

Formulář nutno vyhotovit ve 3 výtiscích – 1x katedra, 1x diplomant, 1x studijní odd. (zašle katedra)

Nejpozději do konce 2. týdne výuky v semestru odešle katedra 1 kopii zadání DP na studijní oddělení a provede zápis údajů týkajících se DP do databáze KOS.
DP zadává katedra nejpozději 1. týden semestru, v němž má student DP zapsanou.

Abstract

Cocciopesto is a very old and interesting material, when by a simple mixing of crushed bricks with water and lime, we get a mortar of similar properties to modern concrete. This quality had already been extensively exploited in the Roman Empire. A chemical nature of the processes was unknown to them of course, but they knew by an experience that the brick dust had a very positive influence on a consistency and strength of the mortar.

Nowadays, with a deeper knowledge of the processes taking place in the mortar, we come back to the use of this material. We try to re-exploit its amazing properties, such as self-healing of cracks, especially for a restoration of historic monuments and a protection of structures in seismic areas.

The thesis, you are reading right now, is devoted to numerical simulations of masonry structures with the cocciopesto mortar joints. It defines an influence of the joint thickness and determines the material properties worth changing in order to improve the overall behavior of the structure. The above-mentioned goals make this thesis unique.

Keywords: cocciopesto, pozzolan, crushed brick, C-S-H gel, thick joints, masonry structures, numerical simulation

Abstrakt

Cocciopesto je velmi starý a zajímavý materiál, kdy pouhým smícháním drcených cihel s vodou a vápnem dostáváme maltu obdobných vlastností jako novodobý beton. Této vlastnosti bylo hojně užíváno už ve starověkém Římě. Samozřejmě si nebyli vědomi podstaty chemických procesů, ale pouhou zkušeností věděli, že cihelný prach má velmi pozitivní vliv na soudržnost a pevnost malty.

Dnes, s hlubší znalostí procesů probíhajících v maltě, se vracíme k používání tohoto materiálu. Pokoušíme se znovu využít jeho úžasných vlastností, jako je třeba samo-zacelování trhlin, obzvláště pro restaurování historických památek a ochranu staveb v seismicky aktivních oblastech.

Práce, kterou právě teď čtete, je věnována numerickým simulacím zděných konstrukcí se spárami z malty cocciopesto. Určuje vliv tloušťky spár a stanovuje materiálové vlastnosti, které má smysl měnit z důvodu zlepšení celkové odezvy konstrukce. Výše zmíněné cíle dělají tuto práci ojedinělou.

Klíčová slova: cocciopesto, pucolán, drcená cihla, C-S-H gel, tlusté spáry, zděné konstrukce, numerické simulace

Contents

Contents **5**

Introduction **8**

1 Cocciopesto **10**

1.1 Mortars 11

1.2 Chemistry 11

1.3 Properties 13

2 Goals **15**

3 Finite Element Method **16**

3.1 Introduction 16

3.2 Principles of FEM 16

3.2.1 Linearity 17

3.3 Discrete Elements - 1D 18

3.4 Continuum Elements - 2D and 3D 18

3.4.1 Simplex, Complex and Multiplex Elements 18

3.4.2 Inter-Element Compatibility 19

3.4.3 Convergence 20

3.4.4 Aspect Ratio 20

3.5 Elasticity Equations 21

3.5.1 Kinematic equations 21

3.5.1.1 Displacements 21

3.5.1.2 Strains 22

3.5.2 Equilibrium Equations 23

3.5.3 Constitutive Equations 25

3.6 Governing Equations of FEM 27

4 Methods Used by ATENA **30**

4.1 Material Model 30

4.1.1 Model Formulation 31

4.1.2 Fracture Model 32

4.1.3 Plasticity Model 33

4.2 Solution of Non-Linear Equations 36

4.2.1 Full Newton-Raphson Method 36

4.2.2 Modified Newton-Raphson Method 39

4.2.3 Arc-Length Method 39

4.2.4 Line Search Method 40

5 Numerical Simulations 42
5.1 Numerical Model 42
5.2 Setting of ATENA 43
5.2.1 Materials 44
5.2.2 Solution Parameters 45
5.2.3 Meshing 46
5.2.4 2D analysis vs. 3D analysis 47
5.3 Influence of Geometry 50
5.3.1 Thickness of Joints 50
5.3.2 Head Joints 55
5.4 Influence of Material Properties 60
5.4.1 Young's Modulus 60
5.4.2 Fracture Energy 62
5.4.3 Tensile Strength 65
5.4.4 Compressive Strength 67
6 Conclusion 69
References 70

Introduction

The term cocciopesto is used for mortars made with a crushed brick or terracotta. Sometimes the term "opus signinum" is used instead. The first notes about exploiting the cocciopesto can be traced to the times of old Phoenicians and subsequently this type of mortar spread among other nations, which were in contact with them. As time went, a thickness of the joints increased together with dimensions of the brick fragments and an aggregate. Later on, the thickness of the joints became even greater than the thickness of the bricks. For example, the mortar joint thickness was 70 mm in the Hagia Sofia in Istanbul. The reason why this was not satisfactorily explained up to these days is not surprising. Despite a comprehensive research of a literature, there were found no numerical simulations focused on a characteristic behavior of thick cocciopesto joints used in masonry structures.

Hagia Sophia mortar sample [9]

Of course, there are many simulations dealing with masonry structures, but the problem is that simplifications of the models often make observing the joints impossible. For example, Zucchini, Lourenço (2009) [1] use a homogenization utilizing a periodic repetition of the microstructure (masonry bond), which permits to establish constitutive relations in terms of averaged stresses and strains. It is very useful, because it is then possible to use standard material models and software codes for isotropic materials, but it is not possible to study the joints in such a homogenized monolithic material. Another example is determining a response of a brick-mortar connection by substituting the joints by interface elements as e.g. Lotfi, Shing (1994) [2], Gambarotta, Lagomarsino (1997) [3], Lourenço, Rots (1997) [4], Senthivel, Lourenço (2009) [5]. Again, it is impossible to capture the behavior of the joints, as well as in the case of Brasile, Casciaro, Formica (2007) [6], who described the bricks as rigid bodies and the mortar joints as non-linear interface springs.

Therefore, one of the main goals of this thesis is to determine the role of the thick joints in the behavior of masonry structures, by means of the direct numerical simulation. After this, a parametric study of several important material properties of the cocciopesto mortar is done. It should help to define which material properties influence the overall response favorably and then implicitly set the best mix ratios of the mortar.

From the reasons mentioned above, this thesis is not improving or extending any research or simulation, because there are no similar results available, to the best of

our knowledge. Therefore, this work can be considered as a pioneering one in this particular issue.

The first chapter is devoted to the description of the basic chemical processes leading to the extraordinary characteristics of the cocciopesto mortars, and it also explains what causes such characteristic properties. The second chapter set the more detailed goals of this work. The third one deals with the principle of the finite element method, its origin and its properties, but also with elasticity equations that help to understand governing equations of FEM, which are included in this chapter too. Chapter number four describes a choice of suitable FEM software and its material models and solution methods. The fifth chapter works with data from the numerical simulations and analyzes them. Finally, the last, sixth, chapter summarizes the obtained results and findings.

1 Cocciopesto

Cocciopesto is well known as a material used for a waterproof lining in ancient cisterns and it is used from 2nd century B.C. The Romans used crushed brick wherever they needed waterproof mortar and the natural pozzolans were not available. Historians as Vitruvius recommended mixing crushed bricks with mortar to improve its mechanical properties. In times of Byzantine Empire, the cocciopesto mortars ceased to be used only as water insoluble material, but also as joints of load-bearing structures. A texture of the cocciopesto mortar is shown in Figure 1.1.

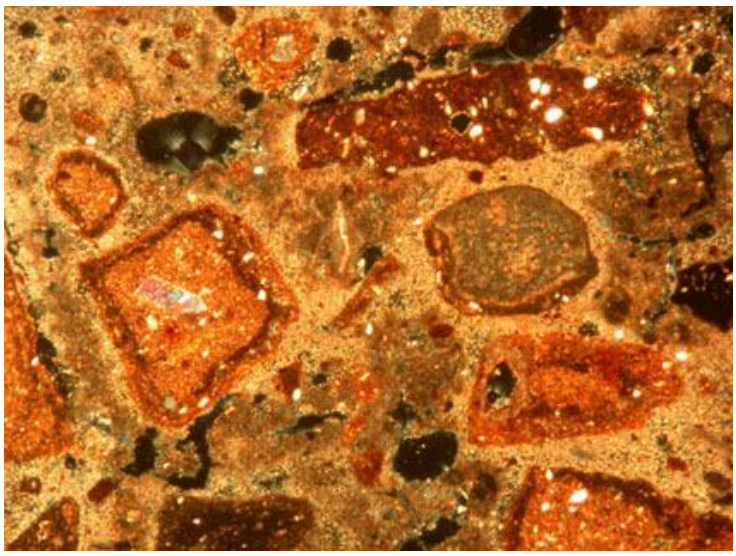

Fig. 1.1: Fragments of crushed terracotta in a cocciopesto [10]

Cocciopesto often contains so-called pozzolana as well. Pozzolana can be either natural (volcanic minerals) or an industrial by-product (e.g. pulverized fly ash, metakaolin) with an amorphous or a partially crystalline structure. Pozzolans themselves do not react, and therefore do not harden, after mixing with water. But if finely powdered, they can together with water and calcium hydroxide ($Ca(OH)_2$) contained in lime mortars, obtain a certain mechanical strength. The reaction between lime and pozzolans is actually similar to a reaction in portland cement because in both cases an amorphous C-S-H[1] (Calcium-Silicate-Hydrate) gel is formed.

[1] Abbreviated symbols used in the cement chemistry: CaO = C; SiO_2 = S and H_2O in hydrated cement is denoted by H.

1.1 Mortars

Mortars have two important roles in civil engineering in these days, as well as they had a long time ago. First one is to connect structural elements, mostly stones, and bricks and second one is a protective function as a plaster of structures.

Mortars are generally divided according to the material they are based on (e.g. lime, gypsum, clay binders, etc.)

Since pozzolanic materials need to be mixed with calcium hydroxide ($Ca(OH)_2$), we are going to focus on the lime mortars. The lime used in mortars can be classified into two groups. Non-hydraulic (or air) lime, which does not need water for hardening, and hydraulic lime. Nowadays, the term *hydraulic* includes cements and other bonding agents, which set and harden as a result of chemical reactions with water.

The main properties of the cocciopesto mortars, i.e. lime mortars with pozzolans/crushed bricks, are the following:

- superior mechanical strength to lime mortars
- certain capacity of deformation
- low resistance to unfavorable climatic conditions
- scarce presence of soluble salts
- lower permeability to water than lime mortars [7]

Generally, we can say that cocciopesto mortars are weaker and more porous in comparison with portland cement mortars. These characteristics can be advantageous in some cases, mainly due to better compatibility with other building materials. This is an extremely important factor when dealing with historic monuments. However, as it has been already mentioned, both types of mortars have a common component from mineralogical and chemical point of view and it is the amorphous C-S-H gel.

1.2 Chemistry

Hydraulic mortars harden by chemical reactions between calcium hydroxide ($Ca(OH)_2$) and reactive silicates and aluminates in the presence of water. In natural hydraulic limes, the reactive silicates and aluminates are supplied by clay minerals in the limestone. Where a hydraulic set (hydraulic set are active clay particles, lime, and water) is required in a lime mortar and these minerals are not naturally present, or are not present in sufficient quantities, they can be added in the form of the pozzolans or the brick powder [11].

The pozzolanic activity of a material is defined as its ability to react with $Ca(OH)_2$, in the presence of water. The pozzolanic activity of a ceramic powder depends on the chemical and mineralogical composition of the initial clay (a high content of clay supports the pozzolanic activity), and the thermal treatment. Furthermore, the final characteristics of the ceramic powder that influence the pozzolanic activity are mainly the amorphous phase content and the specific surface [12].

Bricks, or more precisely clay minerals, have a very good pozzolanic activity if they are burnt at temperatures from 600 °C to 900 °C and sufficiently ground. The temperature higher than 600 °C is necessary to lose water from silica and alumina, resulting in a demolition of a crystalline network and these amorphous substances can react with water and hydrated lime. However, the temperature cannot be higher than 900 °C, because then high temperature crystals are formed. Finally, the sufficient grinding is necessary to reach a big specific surface and subsequently big contact area between materials.

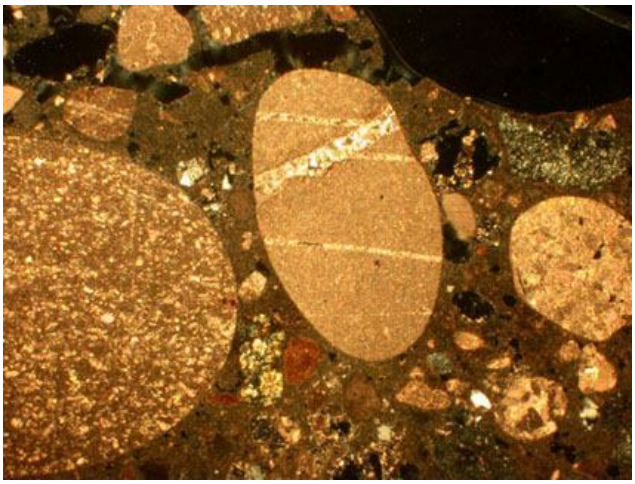

Fig. 1.2: Limestone pebbles as aggregates in non-hydraulic mortar [10]

In simple non-hydraulic lime mortars, this hardening is supplemented by drying and carbonation that is by the conversion of calcium hydroxide ($Ca(OH)_2$) to calcium carbonate ($CaCO_3$) by reaction with atmospheric carbon dioxide (CO_2) [11]. Then the individual particles in non-hydraulic mortar look like simply put together without any reaction rims (see Figure 1.2), on the contrary to cocciopesto (see Figure 1.3).

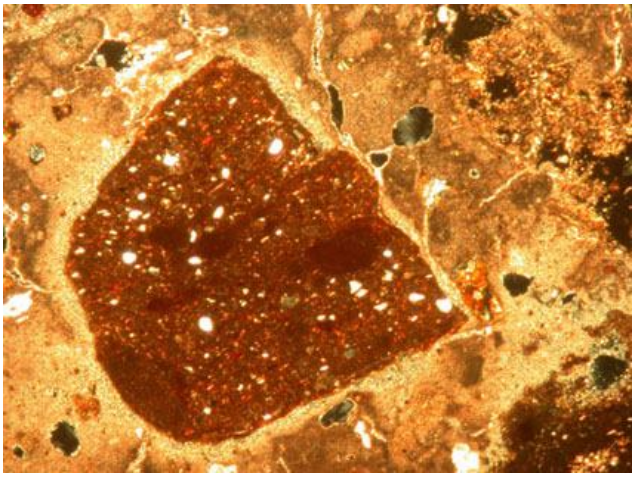

Fig. 1.3: Fragment of pottery in cocciopesto with light reaction rim [10]

The pozzolanic character of the crushed brick mortar is caused by the adhesion reactions of physico-chemical character occurring at the ceramic-matrix interface. The observed reactions could be attributed to calcium silicate (Ca_2SiO_4) formations at the interface along the brick fragment, acting as the silicate source and the lime, which makes the interfacial surface alkaline and causes the chemical reaction. The penetration of lime into the ceramic and the consequent reaction transforms the microstructure of the ceramic by transforming the pore radii into smaller pores, decreasing the total porosity, and augmenting the apparent density. The reduction of the pore radii confirms the cementitious character of the mortar matrix, giving high strength to the mortar [8]. The chemical principle of the cocciopesto is simply summarized in a following scheme.

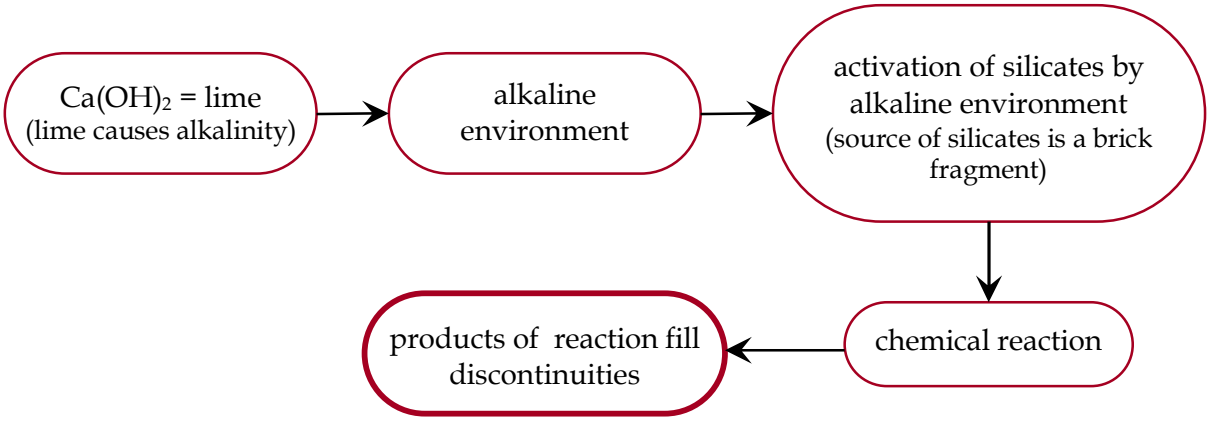

Fig. 1.4: Summary of chemical principle

1.3 Properties

The mortars from Hagia Sofia have relatively high strength together with very high durability. These mortars also turned out to be resistant to continuous stresses and strains thanks to the presence of the amorphous C-S-H gel at interfaces between crushed brick powder and binder. C-S-H gel occurs in the binding matrix as well. These properties allow for better energy absorption during an earthquake, without a creation of fractures [9].

The reaction product fills the discontinuities of the structure, thus eliminating any breaks in continuity between the mortar and the brick as illustrated by Figure 1.5. Small fragments of brick also seem, in turn, to penetrate the adjacent mortar [13]. This transformation matches with the hydraulic character of the mortar matrix, providing the mortar high physico-chemical resistance to polluted and marine atmosphere [14].

In the case of large sized brick pebbles (even if reaction layers can be detected along the contact surface between the binder and the pebbles) the reaction cannot penetrate very far into the pebble. Hence, the reaction can only realize a better adhesion between the binder and the aggregate [13].

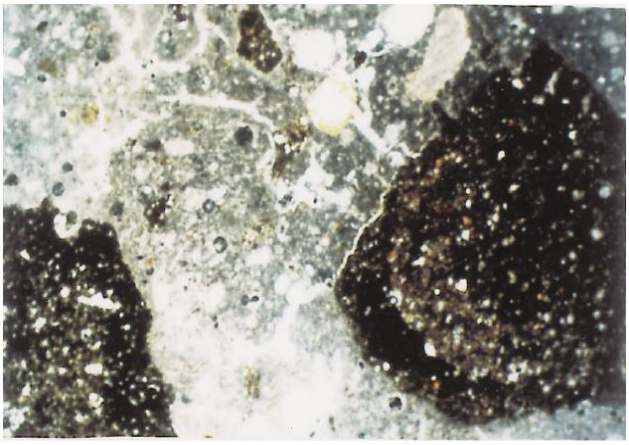

Fig. 1.5: Ceramic fragments rounded by reaction rims in the matrix [14]

In addition, there is one more extremely interesting fact about the cocciopesto mortars. There were cracks observed by an optical microscope, going through the brick fragments and the matrix, which were filled with a secondary crystallized material. It actually means that there is something like a self-healing effect, treating the damages after an earthquake.

2 Goals

Goals of the thesis are as follows:

- study the issue of the cocciopesto mortars
- study the principles of the FEM
- choose the appropriate FEM program and solver
- study the computation routines of the chosen FEM program and solver
- determine the influence of the thick cocciopesto mortar joints on the behavior of the masonry structures
- investigate the role of the individual material parameters of the cocciopesto mortar in the overall structural response
- interpret the results

3 Finite Element Method

The finite element method is really the famous one in nowadays. Nevertheless, this chapter is not dedicated only to the well-known equations, but above all, it contains explanations and descriptions of the methods in behind, the principles occurring in FEM, its origin etc.

3.1 Introduction

This method was not developed by a single man, but by the participation of many researchers during 2nd half of 20th century e.g. R. Courant, S. Levy, M. J. Turner, O. C. Zienkiewicz, K. J. Bathe etc.

Problem that actually gave rise to this method was that by analyzing the individual members, the results were too conservative providing a design with bigger and heavier members than was necessary. This procedure was used in civil structures, where weight is usually not the main constraint. Analysis of the complete structure was demanded by the need for a better estimation of stresses in the design of airplanes with minimum factor of safety, and consequently minimum weight, during World War 2.

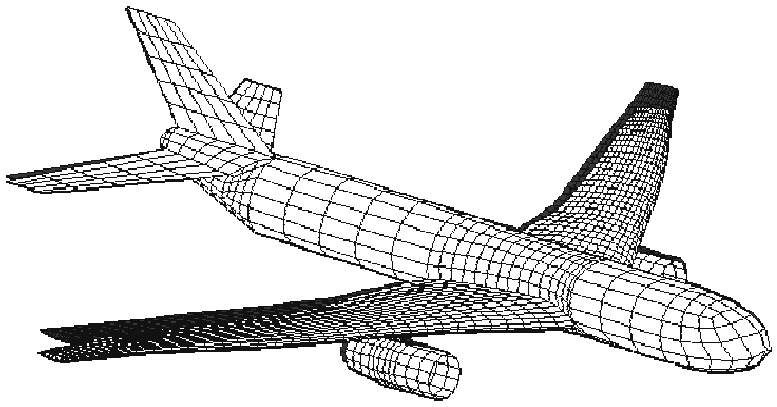

Fig. 3.1: Analysis of loading by a wind blast [16]

3.2 Principles of FEM

The finite element method was initially developed as matrix method of structural analysis for discrete structures (trusses and frames). Later, it also extended for continuum structures, to get better estimation of stresses and deflections even in components with variable cross-section, as well as with heterogeneous and anisotropic materials, allowing for optimum design of complicated components.

The finite element method is a generalized method, based on conventional theory of elasticity (force equilibrium and compatibility of displacements), variational principles, and energy theorems and it is applicable to all types of structures – discrete as well as continuum [15].

This method can produce a huge set of simultaneous equations, which represent load-displacement relationship and it is the reason why the matrix notation is ideal for computerizing. Therefore, development of numerical methods and availability of computers enabled growth of matrix method.

Generally, in FEM the actual component is replaced by a simplified model, identified by a finite number of elements connected at nodes. Each element has an assumed behavior or response to applied loads and the unknown field variables are evaluated at the nodes. The finite element method is an extension of Rayleigh-Ritz method [2], eliminating the difficulty of dealing with a large polynomial representing a suitable displacement field valid over the entire structure.

FEM has a very important property. It is based on minimum potential energy theorem [3] and therefore it converges to the correct solution from a higher value as the number of elements in the model increases. Because a number of elements used in model is selected by an engineer, based on the required accuracy of solution as well as the availability of computer with sufficient memory, this property ensures that the solution is always on the safe side even with lesser number of elements.

The Rayleigh-Ritz method and potential energy approach are now of only academic interest. For a complex problem, it is difficult to deal with a polynomial having as many coefficients as the number of DOF [15].

3.2.1 Linearity

Linear analysis is based on linear stress-strain relationship and is usually permitted when stress at any point is below the elastic limit. In this analysis, linear superposition of results obtained for individual loads is valid.

In many cases, the mathematical formulations are based on small deflection theory. A component with large deflections due to loads, such as aircraft wing, belongs to the category of geometric non-linearity. In these problems, geometry of the component is redefined after every load step by adding the displacements at various nodes to the nodal coordinates, for defining the true geometry to be used for the next load step.

In some aerospace applications, where the component is designed for single use, stress level above yield point, where stress-strain relationship is non-linear, may be allowed. In some other cases involving non-metallic components, material may exhibit non-linear stress-strain behavior in the operating load range. These two cases

[2] This method involves choosing a displacement field over the entire component, usually in the form of a polynomial function, and evaluating unknown coefficients of the polynomial for minimum potential energy [15].

[3] Among all possible kinematically admissible displacement fields (satisfying compatibility and boundary conditions) of a conservative system, the one corresponding to stable equilibrium state has minimum potential energy [17].

belong to the category of material non-linearity. In these problems, total load on the component is applied in small steps and non-linear stress-strain relationship (usually represented by the value of Young's modulus) is considered as linear in each load step. These values are suitably modified after each load step, until the entire load range is covered.

3.3 Discrete Elements - 1D

A discrete structure is assembled from a number of 1D bar elements. Nodes are chosen at the junctions of two or more discrete members, at junctions of two different materials or at points of load application. In 1D element, the axial dimension is very large compared to the cross-section and load is assumed to act uniformly over the entire cross-section. Therefore, the displacement is taken as a function of x, along the axis of the member. The function should be continuous over the entire element with no singularities and easily differentiable to obtain strains for calculation of potential energy [15].

Strains in the element are obtained as derivatives of the displacement polynomial, and therefore they are expressed in terms of the nodal displacements. Stresses are expressed in terms of strains, using the physical equations. By equating work done by external forces to the work done by internal forces (or internal strain energy) of the element and applying variational principle, load-displacement relationship of the element is obtained. They represent a system of simultaneous equations in terms of nodal loads and nodal displacements [15].

3.4 Continuum Elements - 2D and 3D

When one of the cross-sectional dimensions (width) is significant with respect to the length of the member, while the thickness is very small, it is considered as a 2D element. In the case of discrete structures, when each member is treated as a 1D element, the choice of the junctions for nodes is clear. However, in the case of continuum, which is modeled by 2D or 3D elements, there is no unique finite element model for analysis. Each engineer may use a particular number of nodes and a particular orientation of elements. Generally, we can say that a model with less number of higher order elements (with more than two nodes along edges of the elements, i.e. complex, or multiplex elements, for more information see Section 3.4.1) will give better results than higher number of lower order elements and it is economical in terms of computer memory and time.

3.4.1 Simplex, Complex and Multiplex Elements

Finite elements can be divided into the following groups. The simplex elements are those for which the approximating polynomial consists of constant and linear terms [18]. They can be obtained by joining of n+1 nodes in nD space. In 1D, it is a simple 2-noded bar element, in 2D 3-noded triangular element, in 3D 4-noded

tetrahedron, but they are not limited by three dimensions, therefore it can go on e.g. in 4D, it is 5-noded 5-cell, also known as pentachoron, etc.

The complex elements are those for which the approximating polynomial consists of quadratic, cubic, and higher order terms. The complex elements may have the same shape as the simplex elements but will have additional boundary and, sometimes, internal nodes [18]. These are for example 6-noded triangular element for quadratic model, or 9-noded triangular element for cubic model.

The multiplex elements are those whose boundaries are parallel to the coordinate axes to achieve inter-element continuity, and whose approximating polynomials contain higher order terms [18]. These are for example 4-noded rectangle element for 2D, and 8-noded hexahedron element for 3D.

3.4.2 Inter-Element Compatibility

The polynomial used to represent variation of displacements over the element should ensure compatibility of displacement along the inter-element boundary. If this condition is not satisfied, the boundary of two adjacent elements may overlap or show void on application of external loads. This is illustrated in the Figure 3.2. The inter-element compatibility condition is satisfied when displacement at any point along a common edge, of all elements joining along that edge, is a function of displacements of nodes on that edge.

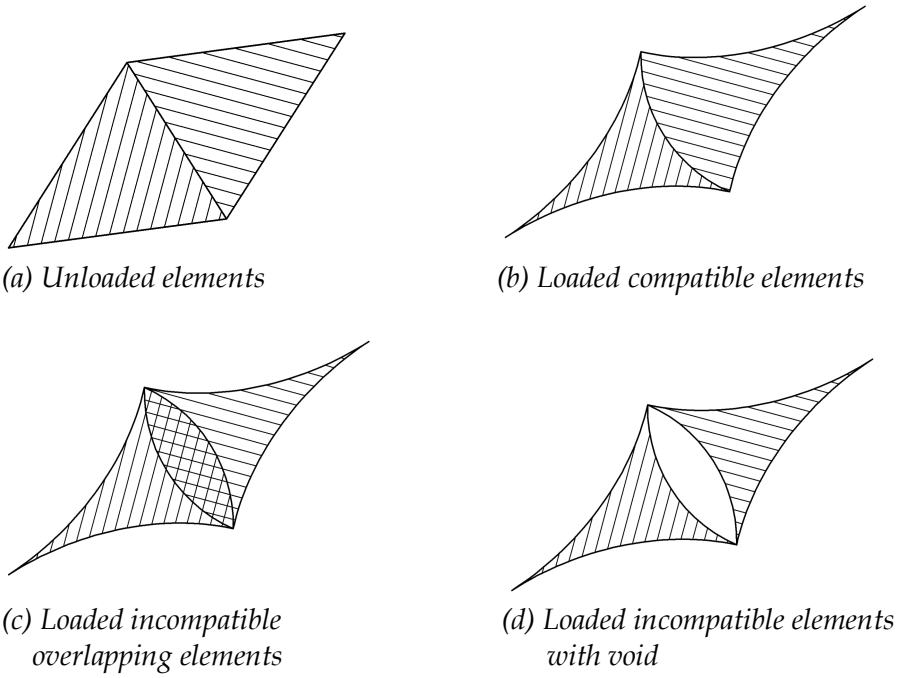

(a) Unloaded elements

(b) Loaded compatible elements

(c) Loaded incompatible overlapping elements

(d) Loaded incompatible elements with void

Fig. 3.2: Examples of (in)compatibilities [15]

3.4.3 Convergence

When we choose a function to represent displacements at any point in the element, it should be ensured that several (convergence) conditions are satisfied.

- The function should be continuous and differentiable (to obtain strains) within the element. This condition is automatically satisfied with polynomial functions.
- The displacement polynomial should include a constant term, representing rigid body displacement, which should occur at any unrestrained component when subjected to external load. It also should contain linear terms, which on differentiation give constant strain terms. Constant strain is the logical condition as the element size reduces to a point in the limit.
- Compatibility of displacements and its derivatives, up to required order, must be satisfied across inter-element boundaries. Otherwise, the displacement solution may result in separated or overlapped inter-element boundaries.
- The polynomial should satisfy geometric isotropy (terms symmetric in terms of coordinate axes x, y, and z). It is very prudent to maintain this isotropy, because than a user of a general-purpose program can start with any particular node of his choice for defining the nodal sequences of different elements of the structure.

3.4.4 Aspect Ratio

Certain conditions are generally specified in the standard packages on the sizes and angles for various elements. Aspect ratio is defined for this purpose as the ratio of the longest side to the shortest side. It is usually limited to 5, and angles are usually limited to 45° - 135° for a triangular element and to 60° - 120° for a quadrilateral of 3D element. Some examples are shown in the Figure 3.3.

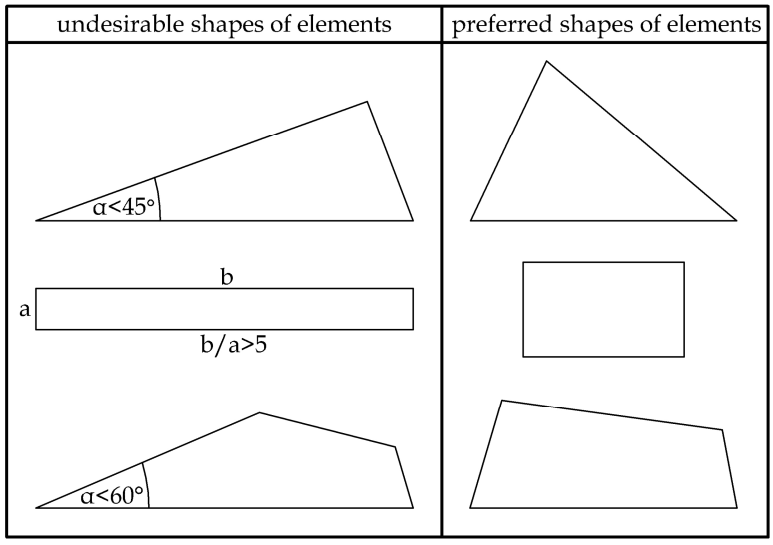

Fig. 3.3: Undesirable and preferred shapes of elements [15]

3.5 Elasticity Equations

First of all, the governing equations of elasticity (for calculation of displacements, strains and stresses) should be summarized. They are valid if the structure undergoes only small deformations and the material behaves in a linearly elastic manner.

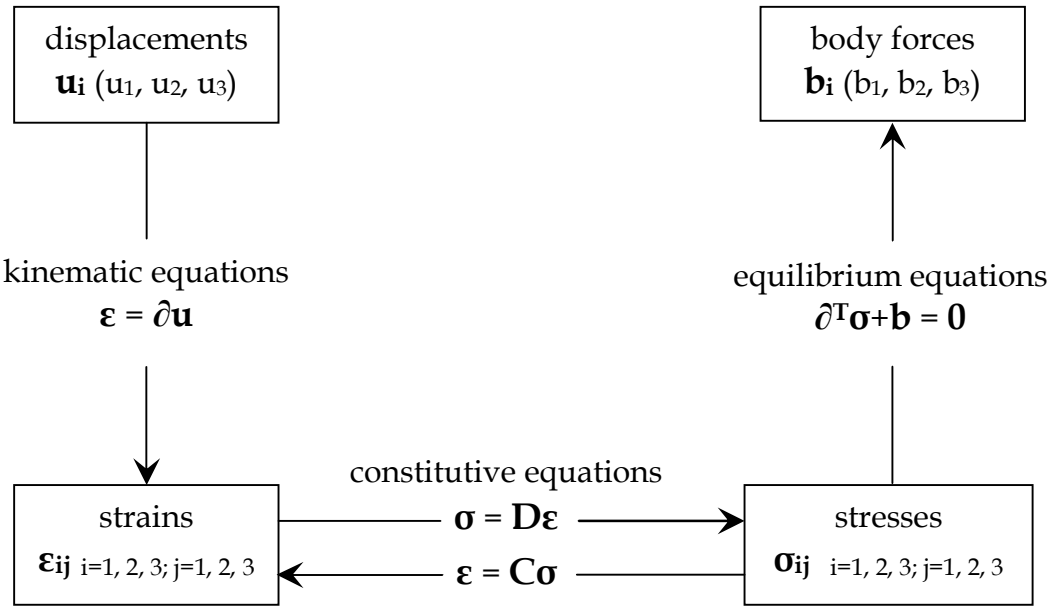

Fig. 3.4: Governing equations of elasticity

3.5.1 Kinematic equations

3.5.1.1 Displacements

The displacements of the points within an elastic body are is described by three components (u, v, w) or (u_1, u_2, u_3), all of them dependent on the position in the Cartesian coordinate system (x, y, z) or (x_1, x_2, x_3). In a matrix notation, the displacements are arranged in a vector as follows

$$\mathbf{u}(\mathbf{x}) = \begin{Bmatrix} u_1(x_1, x_2, x_3) \\ u_2(x_1, x_2, x_3) \\ u_3(x_1, x_2, x_3) \end{Bmatrix} \tag{3.01}$$

while in the index notation the field of displacements can be described as

$$u_i(x_j) \qquad \begin{matrix} i = 1,2,3 \\ j = 1,2,3 \end{matrix} \tag{3.02}$$

3.5.1.2 Strains

Strains describe the deformation of the body. At a point, the stretching, e.g. in the x-direction, can be seen as the differential displacement per unit length. The x-component of strain is then

$$\varepsilon_x = \lim_{\Delta x \to 0} \frac{\Delta u(x,y,z)}{\Delta x} = \frac{\partial u}{\partial x} \tag{3.03}$$

therefore, the normal strain can be understood as a displacement gradient. The distortion of the material, which can be described as the change in originally right angles, is the sum of tilts imparted to vertical and horizontal lines (also called engineering strain)

$$\gamma_{xy} = \gamma_1 + \gamma_2 \approx \tan\gamma_1 + \tan\gamma_2 = \frac{\partial v}{\partial x} + \frac{\partial u}{\partial y} \tag{3.04}$$

For other displacement gradients ε_y, ε_z and distortions γ_{yz}, γ_{zx}, the same reasoning can be applied with cyclic change of coordinates $x \to y \to z \to x$ and displacements $u \to v \to w \to u$.

The strain is a second order tensor and therefore the components can be arranged as follows

$$\boldsymbol{\varepsilon} = \begin{bmatrix} \dfrac{\partial u}{\partial x} & \dfrac{1}{2}\left(\dfrac{\partial u}{\partial y} + \dfrac{\partial v}{\partial x}\right) & \dfrac{1}{2}\left(\dfrac{\partial u}{\partial z} + \dfrac{\partial w}{\partial x}\right) \\ \dfrac{1}{2}\left(\dfrac{\partial u}{\partial y} + \dfrac{\partial v}{\partial x}\right) & \dfrac{\partial v}{\partial y} & \dfrac{1}{2}\left(\dfrac{\partial v}{\partial z} + \dfrac{\partial w}{\partial y}\right) \\ \dfrac{1}{2}\left(\dfrac{\partial w}{\partial x} + \dfrac{\partial u}{\partial z}\right) & \dfrac{1}{2}\left(\dfrac{\partial v}{\partial z} + \dfrac{\partial w}{\partial y}\right) & \dfrac{\partial w}{\partial z} \end{bmatrix} \tag{3.05}$$

where, in the tensorial notation, shear strains (distortions) are halves of the engineering strains. The difference between vectors (first order tensors) and second order tensors shows up in how they transform with respect to coordinate rotations.

The index notation provides a compact description of all the components of three-dimensional states of strain

$$\varepsilon_{ij} = \frac{1}{2}\left(\frac{\partial u_i}{\partial x_j} + \frac{\partial u_j}{\partial x_i}\right) = \frac{1}{2}\left(u_{i,j} + u_{j,i}\right) \tag{3.06}$$

where the comma denotes differentiation with respect to the following spatial variable (partial derivative). This double-subscript index notation leads naturally to a matrix arrangement of the strain components, in which the *i-j* component of the strain becomes the matrix element in the i^{th} row and the j^{th} column

$$\boldsymbol{\varepsilon} = \begin{bmatrix} \varepsilon_{11} & \varepsilon_{12} & \varepsilon_{13} \\ \varepsilon_{21} & \varepsilon_{22} & \varepsilon_{23} \\ \varepsilon_{31} & \varepsilon_{32} & \varepsilon_{33} \end{bmatrix} = \begin{bmatrix} \dfrac{\partial u_1}{\partial x_1} & \dfrac{1}{2}\left(\dfrac{\partial u_1}{\partial x_2} + \dfrac{\partial u_2}{\partial x_1}\right) & \dfrac{1}{2}\left(\dfrac{\partial u_1}{\partial x_3} + \dfrac{\partial u_3}{\partial x_1}\right) \\ \dfrac{1}{2}\left(\dfrac{\partial u_1}{\partial x_2} + \dfrac{\partial u_2}{\partial x_1}\right) & \dfrac{\partial u_2}{\partial x_2} & \dfrac{1}{2}\left(\dfrac{\partial u_2}{\partial x_3} + \dfrac{\partial u_3}{\partial x_2}\right) \\ \dfrac{1}{2}\left(\dfrac{\partial u_3}{\partial x_1} + \dfrac{\partial u_1}{\partial x_3}\right) & \dfrac{1}{2}\left(\dfrac{\partial u_2}{\partial x_3} + \dfrac{\partial u_3}{\partial x_2}\right) & \dfrac{\partial u_3}{\partial x_3} \end{bmatrix} \tag{3.07}$$

Since the strain tensor is symmetric, i.e. $\varepsilon_{ij} = \varepsilon_{ji}$, there are six rather than nine independent strains, as might have been expected [19].

Sometimes it is convenient to arrange the strain components in a vector, or rather pseudovector. Strain is actually a 2nd order tensor, like stress or moment of inertia, and has mathematical properties very different from those of vectors, which must be taken into account while transforming or calculating the norm of strain. The ordering of the elements in the pseudovector is arbitrary, but it is conventional to list them in order (1, 1), (2, 2), (3, 3), (2, 3), (1, 3), (1, 2) [19]. This arrangement yields so-called Voigt notation.

Following the rules of a matrix multiplication, the strain pseudovector can also be written in terms of the displacement vector and proper operator. The strain-displacement relationship can be expressed as

$$\boldsymbol{\varepsilon} = \partial \mathbf{u} \tag{3.08}$$

$$\begin{Bmatrix} \varepsilon_x \\ \varepsilon_y \\ \varepsilon_z \\ \gamma_{yz} \\ \gamma_{xz} \\ \gamma_{xy} \end{Bmatrix} = \begin{bmatrix} \partial/\partial x & 0 & 0 \\ 0 & \partial/\partial y & 0 \\ 0 & 0 & \partial/\partial z \\ 0 & \partial/\partial z & \partial/\partial y \\ \partial/\partial z & 0 & \partial/\partial x \\ \partial/\partial y & \partial/\partial x & 0 \end{bmatrix} \begin{Bmatrix} u \\ v \\ w \end{Bmatrix}$$

3.5.2 Equilibrium Equations

The force equilibrium on an infinitesimal cube results in the following equations (Cauchy's equations)

$$\begin{aligned} \frac{\partial \sigma_x}{\partial x} + \frac{\partial \tau_{yx}}{\partial y} + \frac{\partial \tau_{zx}}{\partial z} + b_x &= 0 \\ \frac{\partial \tau_{xy}}{\partial x} + \frac{\partial \sigma_y}{\partial y} + \frac{\partial \tau_{zy}}{\partial z} + b_y &= 0 \\ \frac{\partial \tau_{xz}}{\partial x} + \frac{\partial \tau_{yz}}{\partial y} + \frac{\partial \sigma_z}{\partial z} + b_z &= 0 \end{aligned} \tag{3.09}$$

where b_i are body forces, such as gravity. These equations can be written using the index notation as

$$\sigma_{ij,j} + b_i = 0 \tag{3.10}$$

In a pseudovector-matrix form we can write

$$\begin{bmatrix} \frac{\partial}{\partial x} & 0 & 0 & 0 & \frac{\partial}{\partial z} & \frac{\partial}{\partial y} \\ 0 & \frac{\partial}{\partial y} & 0 & \frac{\partial}{\partial z} & 0 & \frac{\partial}{\partial x} \\ 0 & 0 & \frac{\partial}{\partial z} & \frac{\partial}{\partial y} & \frac{\partial}{\partial x} & 0 \end{bmatrix} \begin{Bmatrix} \sigma_x \\ \sigma_y \\ \sigma_z \\ \tau_{yz} \\ \tau_{xz} \\ \tau_{xy} \end{Bmatrix} + \begin{Bmatrix} b_x \\ b_y \\ b_z \end{Bmatrix} = \begin{Bmatrix} 0 \\ 0 \\ 0 \end{Bmatrix} \tag{3.11}$$

From the moment equilibrium on the infinitesimal cube, we get

$$\begin{aligned} \tau_{yz} &= \tau_{zy} \\ \tau_{zx} &= \tau_{xz} \\ \tau_{xy} &= \tau_{yx} \end{aligned} \tag{3.12}$$

due to this fact the stress tensor, here in the matrix representation,

$$\boldsymbol{\sigma} = \sigma_{ij} = \begin{bmatrix} \sigma_{11} & \sigma_{12} & \sigma_{13} \\ \sigma_{21} & \sigma_{22} & \sigma_{23} \\ \sigma_{31} & \sigma_{32} & \sigma_{33} \end{bmatrix} \tag{3.13}$$

is also symmetric. The element in the i^{th} row and the j^{th} column of this matrix is the stress on the i^{th} face in the j^{th} direction.

Equilibrium of the stress and surface traction on the boundary can be expressed by Cauchy's formula. It requests the equilibrium of the external traction forces with internal stress. The traction $\boldsymbol{t}$ is associated with any plane with normal n. It is a stress on the surface of the body

$$\mathbf{t} = \lim_{\Delta A \to 0} \frac{\Delta \mathbf{F}}{\Delta A} \tag{3.14}$$

where the externally applied force $\mathbf{F}$ comprises of components in direction of coordinates. Therefore, the traction $\mathbf{t}$ is completely defined by three traction vectors associated with coordinate planes, for instance

$$\mathbf{t}^{(x)} = \begin{Bmatrix} \sigma_x \\ \tau_{xy} \\ \tau_{xz} \end{Bmatrix} \tag{3.15}$$

generally for an arbitrary normal plane n it holds that

$$\mathbf{t}^{(\mathbf{n})} = \mathbf{t}^{(x)} n_x + \mathbf{t}^{(y)} n_y + \mathbf{t}^{(z)} n_z \tag{3.16}$$

which can be written in compact form as

$$\mathbf{t} = \boldsymbol{\sigma}\mathbf{n} \tag{3.17}$$

and in the index notation as

$$t_j^{(n)} = \sigma_{ij} n_i \tag{3.18}$$

where n_i is a multiple of the cosine angle between the investigated plane and coordinate system (it is a projection onto the coordinate axes).

3.5.3 Constitutive Equations

The previous sections deal only with the kinematics (geometry) and static equilibrium of the body, but they do not provide insight on the role of the material itself. The kinematic equations relate strains to displacement gradients, and the equilibrium equations relate stress to the applied tractions on loaded boundaries and provide the relations among stress gradients within the material. Six more equations, relating the stresses to strains are needed, and these are provided by the material's constitutive relations. In this section, isotropic elastic materials are dealt with [19].

In the general case of a linear relation between components of the strain and stress tensors, we might propose a statement of the form

$$\sigma_{ij} = D_{ijkl}\left(\varepsilon_{kl} - \varepsilon_{kl}^{t}\right) \tag{3.19}$$

where D_{ijkl} is a 4th order tensor and ε^t_{kl} is the initial (or eigen / stress-free) strain. Because indices kl do not appear in the equation after summation, they are called "dummy indices". Previous expression constitutes a sequence of nine equations, since each component of σ_{ij} is a linear combination of all the components of $\varepsilon_{kl.}$ For instance

$$\sigma_{23} = D_{2311}\varepsilon_{11} + D_{2312}\varepsilon_{12} + \ldots + D_{2333}\varepsilon_{33} \tag{3.20}$$

Based on each of the indices of D_{ijkl} taking on values from 1 to 3, we might expect 81 independent components in D. However, both the stress tensor and the strain tensor are symmetric ($\sigma_{ij} = \sigma_{ji}$ and $\varepsilon_{ij} = \varepsilon_{ji}$), we must also have $D_{ijkl} = D_{ijlk}$ and

$D_{ijkl} = D_{jikl}$. These relations are called minor symmetries. This reduces the number of D components to 36, as can be seen from a linear relation between the pseudovector forms of the strain and stress [19]

$$\begin{Bmatrix} \sigma_x \\ \sigma_y \\ \sigma_z \\ \tau_{yz} \\ \tau_{xz} \\ \tau_{xy} \end{Bmatrix} = \begin{bmatrix} D_{11} & D_{12} & D_{13} & D_{14} & D_{15} & D_{16} \\ D_{21} & D_{22} & D_{23} & D_{24} & D_{25} & D_{26} \\ D_{31} & D_{32} & D_{33} & D_{34} & D_{35} & D_{36} \\ D_{41} & D_{42} & D_{43} & D_{44} & D_{45} & D_{46} \\ D_{51} & D_{52} & D_{53} & D_{54} & D_{55} & D_{56} \\ D_{61} & D_{62} & D_{63} & D_{64} & D_{65} & D_{66} \end{bmatrix} \begin{Bmatrix} \varepsilon_x \\ \varepsilon_y \\ \varepsilon_z \\ \gamma_{yz} \\ \gamma_{xz} \\ \gamma_{xy} \end{Bmatrix} \tag{3.21}$$

It can be shown that the **D** matrix in this form is also symmetric and therefore it contains only 21 independent elements.

If the material exhibits symmetry in its elastic response, the number of independent elements in the **D** matrix can be further reduced. In the simplest case of an isotropic material, having the same stiffness in all directions, only two elements are independent – for example Young's modulus (E) and Poisson's ratio (ν). From these, so-called shear modulus can be calculated

$$G = \frac{E}{2(1+\nu)} \tag{3.22}$$

If a body is loaded by the stress σ_x, the resulting deformation $\varepsilon_x = \sigma_x / E$ and the other normal components of strain are $\varepsilon_y = \varepsilon_z = -\nu\varepsilon_x = -\nu\sigma_x / E$. In the general stress-state, the other normal strain components are derived analogically (however, the material must be isotropic)

$$\varepsilon_x = \frac{1}{E}\left(\sigma_x - \nu\sigma_y - \nu\sigma_z\right) \tag{3.23}$$

$$\varepsilon_y = \frac{1}{E}\left(-\nu\sigma_x + \sigma_y - \nu\sigma_z\right) \tag{3.24}$$

$$\varepsilon_z = \frac{1}{E}\left(-\nu\sigma_x - \nu\sigma_y + \sigma_z\right) \tag{3.25}$$

In case of isotropic material, each shear deformation is proportional to the corresponding shear stress with the constant of proportionality $1/G$

$$\gamma_{xy} = \frac{\tau_{xy}}{G} = \frac{2(1+\nu)}{E}\tau_{xy} \tag{3.26}$$

$$\gamma_{xz} = \frac{\tau_{xz}}{G} = \frac{2(1+\nu)}{E}\tau_{xz} \tag{3.27}$$

$$\gamma_{yz} = \frac{\tau_{yz}}{G} = \frac{2(1+\nu)}{E}\tau_{yz} \tag{3.28}$$

The six above equations can be written in the matrix form as

$$\begin{Bmatrix} \varepsilon_x \\ \varepsilon_y \\ \varepsilon_z \\ \gamma_{yz} \\ \gamma_{xz} \\ \gamma_{xy} \end{Bmatrix} = \frac{1}{E}\begin{bmatrix} 1 & -\nu & -\nu & 0 & 0 & 0 \\ -\nu & 1 & -\nu & 0 & 0 & 0 \\ -\nu & -\nu & 1 & 0 & 0 & 0 \\ 0 & 0 & 0 & 2(1+\nu) & 0 & 0 \\ 0 & 0 & 0 & 0 & 2(1+\nu) & 0 \\ 0 & 0 & 0 & 0 & 0 & 2(1+\nu) \end{bmatrix}\begin{Bmatrix} \sigma_x \\ \sigma_y \\ \sigma_z \\ \tau_{yz} \\ \tau_{xz} \\ \tau_{xy} \end{Bmatrix} \tag{3.29}$$

which can be written in compact form as

$$\boldsymbol{\varepsilon} = \mathbf{C}\boldsymbol{\sigma} \tag{3.30}$$

where **C** is the elastic compliance matrix. By inversion, we get the generalize Hook's law

$$\boldsymbol{\sigma} = (\mathbf{C})^{-1}\boldsymbol{\varepsilon} = \mathbf{D}\boldsymbol{\varepsilon} \tag{3.31}$$

where

$$\mathbf{D} = \frac{E}{(1+\nu)(1-2\nu)}\begin{bmatrix} 1-\nu & \nu & \nu & 0 & 0 & 0 \\ \nu & 1-\nu & \nu & 0 & 0 & 0 \\ \nu & \nu & 1-\nu & 0 & 0 & 0 \\ 0 & 0 & 0 & 0{,}5-\nu & 0 & 0 \\ 0 & 0 & 0 & 0 & 0{,}5-\nu & 0 \\ 0 & 0 & 0 & 0 & 0 & 0{,}5-\nu \end{bmatrix} \tag{3.32}$$

is the elastic stiffness matrix of an isotropic material.

3.6 Governing Equations of FEM

Firstly, suitable basis functions **N** for an approximation of displacements are chosen. The **d** coefficients of these functions are the unknowns of the task and they also scale the value of the basis functions at the nodes.

To express strains from approximated displacements, the kinematic equations are used as usually. Afterwards, stress is calculated from approximated strain using the standard constitutive equations.

The change comes when body force should be calculated from approximated stress, because the equilibrium equations are not used. The equilibrium conditions

are expressed by means of a variational principle (minimum potential energy, virtual work, etc.) and we get so-called weak solution.

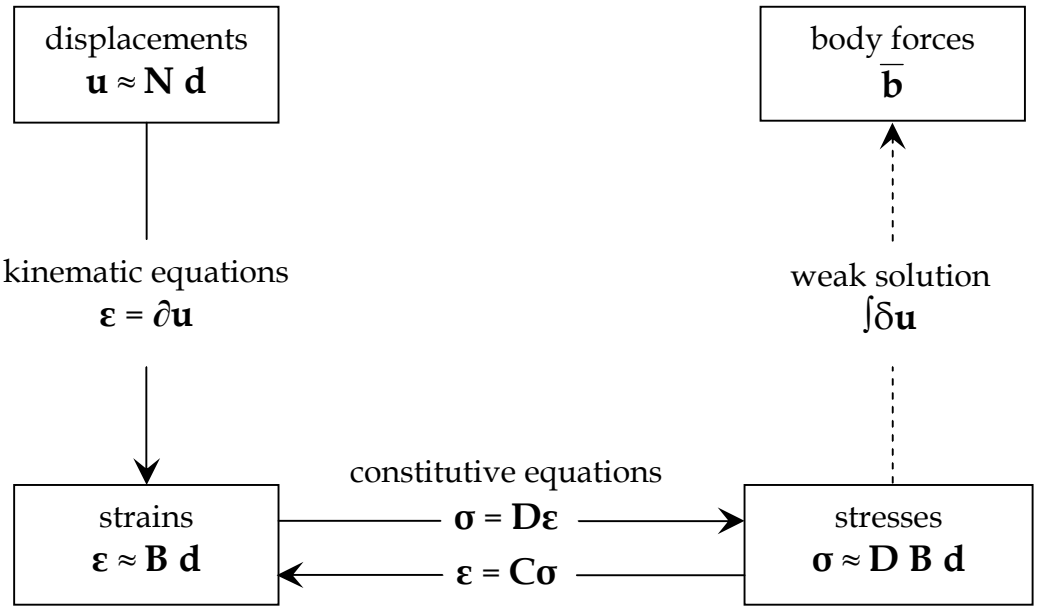

Fig. 3.5: Governing equations of finite element method

Before it is approached to a derivation of the weak solution, it is useful to recall the per-partes integration, which says that

$$\int_o^L \frac{\mathrm{d}}{\mathrm{d}x} f(x)\, g(x)\, \mathrm{d}x = [f(x)\, g(x)]_o^L - \int_o^L f(x) \frac{\mathrm{d}}{\mathrm{d}x} g(x)\, \mathrm{d}x \tag{3.33}$$

where $f(x)$ and $g(x)$ are arbitrary functions. The first term of the right-hand side can be expressed as

$$\begin{aligned} [f(x)\ g(x)]_o^L &= f(\mathrm{L})\ g(\mathrm{L}) - f(0)\ g(0) = f(\mathrm{L})\ g(\mathrm{L})\ n(\mathrm{L}) + f(0)\ g(0)\ n(0) = \\ &= \int_\Gamma f(x)\ g(x)\ n(x)\ \mathrm{d}x \end{aligned} \tag{3.34}$$

where n is a unit normal vector of an arbitrary plane and Γ is a boundary of the element. After back-substitution and generalization we get

$$\int_\Omega (\partial \mathbf{f})^T\ \mathbf{g}\ \mathrm{d}\Omega = \int_\Gamma \mathbf{f}^T \mathbf{g}\ \mathbf{n}\ \mathrm{d}\Gamma - \int_\Omega \mathbf{f}^T\ \partial^T \mathbf{g}\ \mathrm{d}\Omega \tag{3.35}$$

where Ω is a volume of the element and ∂ is a differential operator. The knowledge can be applied on the expression of the work done by internal forces (or internal

strain energy), but if standard strain is replaced by *virtual* strain, we get *virtual* work done by internal forces.

$$\begin{aligned}\int_\Omega \delta\boldsymbol{\varepsilon}^T\,\boldsymbol{\sigma}\,\mathrm{d}\Omega &= \int_\Omega (\partial\,\delta\mathbf{u})^T\boldsymbol{\sigma}\,\mathrm{d}\Omega = \int_\Gamma \delta\mathbf{u}^T\boldsymbol{\sigma}\,\mathbf{n}\,\mathrm{d}\Gamma - \int_\Omega \delta\mathbf{u}^T\,\partial^T\boldsymbol{\sigma}\,\mathrm{d}\Omega = \\ &= \int_\Gamma \delta\mathbf{u}^T\,\mathbf{t}\,\mathrm{d}\Gamma - \int_\Omega \delta\mathbf{u}^T\,(-\overline{\mathbf{b}})\,\mathrm{d}\Omega = \\ &= \int_{\Gamma^u} \delta\mathbf{u}^T\,\mathbf{t}\,\mathrm{d}\Gamma + \int_{\Gamma^t} \delta\mathbf{u}^T\,\bar{\mathbf{t}}\,\mathrm{d}\Gamma + \int_\Omega \delta\mathbf{u}^T\,\overline{\mathbf{b}}\,\mathrm{d}\Omega\end{aligned} \tag{3.36}$$

Where $\boldsymbol{\sigma}$ is stress tensor, $\delta\boldsymbol{\varepsilon}$ is virtual strain tensor, $\delta\mathbf{u}$ is virtual displacement vector, $\overline{\mathbf{b}}$ is prescribed body force vector, $\mathbf{t}$ is surface traction vector and $\bar{\mathbf{t}}$ is prescribed surface traction vector.

Since it is required for Γ^u that $\delta\mathbf{u} = \mathbf{0}$ we get

$$\int_{\Gamma^u} \delta\mathbf{u}^T\,\mathbf{t}\,\mathrm{d}\Gamma = 0 \tag{3.37}$$

and the equation (3.36) can be simplified to the form

$$\int_\Omega \delta\boldsymbol{\varepsilon}^T\,\boldsymbol{\sigma}\,\mathrm{d}\Omega = \int_{\Gamma^t} \delta\mathbf{u}^T\,\bar{\mathbf{t}}\,\mathrm{d}\Gamma + \int_\Omega \delta\mathbf{u}^T\,\overline{\mathbf{b}}\,\mathrm{d}\Omega \tag{3.38}$$

Now, with the knowledge of the governing equations of FEM, it is possible to substitute into the equation (3.38) as

$$\int_\Omega (\mathbf{B}\,\delta\mathbf{d})^T\mathbf{D}\,\mathbf{B}\,\mathbf{d}\,\mathrm{d}\Omega = \int_{\Gamma^t} (\mathbf{N}\,\delta\mathbf{d})^T\,\bar{\mathbf{t}}\,\mathrm{d}\Gamma + \int_\Omega (\mathbf{N}\,\delta\mathbf{d})^T\,\overline{\mathbf{b}}\,\mathrm{d}\Omega \tag{3.39}$$

After small rearrangement we get

$$\int_\Omega \delta\mathbf{d}^T\,\mathbf{B}^T\mathbf{D}\,\mathbf{B}\,\mathrm{d}\Omega\,\mathbf{d} = \int_{\Gamma^t} \delta\mathbf{d}^T\,\mathbf{N}^T\,\bar{\mathbf{t}}\,\mathrm{d}\Gamma + \int_\Omega \delta\mathbf{d}^T\,\mathbf{N}^T\,\overline{\mathbf{b}}\,\mathrm{d}\Omega \tag{3.40}$$

Now it is clearly visible, that the equation (3.40) can be simply rewritten as

$$\mathbf{K}\mathbf{d} = \mathbf{f}_{ext} \tag{3.41}$$

where $\mathbf{K}$ is the stiffness matrix and $\mathbf{f}_{ext}$ is external force vector.

The discretized weak form gives a set of linear algebraic equations. The discrete nodal displacements $\mathbf{d}$ are the solution to these equations.

4 Methods Used by ATENA

After several consultations with my supervisor and prof. Petr Kabele, the ATENA software by Červenka Consulting, s.r.o. was chosen as the suitable code for non-linear simulation of masonry. The ATENA has a realistic model for concrete, including development of cracks. It has been tested successfully many times and the development of the software lasts several tens of years. Of course, this thesis deals with mortars and not with concrete, but it has been proven e.g. by Šejnoha et al. (2008) [20] that the advanced model for concrete is very well suited even for mortars modeling.

In this chapter, the methods and the models used by the ATENA are described, since their knowledge is fundamental for the correct use, as well as the basic knowledge of the finite element method, described in Chapter 3.

4.1 Material Model

The model used in the thesis, 3D non-linear cementitious model, is probably the most powerful model for concrete implemented in the ATENA. Detailed description of this model is available in Červenka, Papanikolaou (2008) [21]. This section is a summary of that paper with some additional explanations. Therefore, for simplicity, this reference will not be indicated throughout the section anymore.

It is a 3D constitutive model, combining fracture and plasticity. Fracture is modeled by the Rankine tensile criterion. A hardening and softening plasticity model, based on the Menétrey, Willam (1995) [22] three-parameter failure surface, is used to simulate concrete crushing. The plastic-damage models usually consider an isotropic damage formulation, which neglects the anisotropic nature of cracked concrete behavior. In this model, the cracked concrete is modeled as an orthotropic material and it considers the problematic of physical changes e.g. crack closure. In addition, it considers the shear behavior of cracked concrete and rotated as well as fixed crack formulation.

The difference between rotated and fixed crack models is that in the case of the rotated crack model, the cracks rotate as the direction of the principal stress changes and therefore the crack is always normal to the principal tensile stress direction. The fixed crack model is obtained if the cracks are normal to the principle tensile stress at the moment of crack initiation and their direction do not change during the subsequent growth even when the direction of the principal stress changes. From this reason, it is possible to set fixed crack model coefficient in ATENA. Its value determines at which maximum residual tensile stress level the crack direction gets fixed. In other words, 0,0 means fully rotated crack model, 1,0 fixed since cracking starts. Values between 0,0 and 1,0 determine the level, e.g. 0,7 fixes the crack direction from the moment it opens, till the softening law drops to 0,7 times the initial tensile strength (more about softening in Section 4.1.3).

4.1.1 Model Formulation

The material model formulation assumes small strains and it is based on the strain decomposition, which can be written as

$$\dot{\boldsymbol{\varepsilon}} = \dot{\boldsymbol{\varepsilon}}_e + \dot{\boldsymbol{\varepsilon}}_p + \dot{\boldsymbol{\varepsilon}}_f \tag{4.01}$$

where $\dot{\boldsymbol{\varepsilon}}$ is the total strain rate, $\dot{\boldsymbol{\varepsilon}}_e$ is the elastic strain rate, $\dot{\boldsymbol{\varepsilon}}_p$ is the plastic strain rate and $\dot{\boldsymbol{\varepsilon}}_f$ is the fracture strain rate.

The stress development can be then defined by the following rate equations describing the progressive degradation (cracking) and plastic yielding (crushing)

$$\dot{\boldsymbol{\sigma}} = \mathbf{D}\dot{\boldsymbol{\varepsilon}}_e = \mathbf{D}(\dot{\boldsymbol{\varepsilon}} - \dot{\boldsymbol{\varepsilon}}_p - \dot{\boldsymbol{\varepsilon}}_f) \tag{4.02}$$

The plastic strain rate $\dot{\boldsymbol{\varepsilon}}_p$ is evaluated from the plasticity flow rule

$$\dot{\boldsymbol{\varepsilon}}_p = \dot{\lambda}_p \mathbf{g}_p(\boldsymbol{\sigma}), \qquad \dot{\lambda}_p \geq 0 \tag{4.03}$$

where $\dot{\lambda}_p$ is a plastic multiplier rate, which expresses the rate of plastic deformation and $\mathbf{g}_P(\boldsymbol{\sigma})$ is matrix with six components, which are functions of an instantaneous stress state, and define a ratio of individual components of plastic strain rate. In the case of *associative* plasticity, the $\mathbf{g}_P(\boldsymbol{\sigma})$ matrix is *associated* with a plasticity function f_P in such a way that it is its a gradient. Then the equation (4.03) can be rewritten as

$$\dot{\boldsymbol{\varepsilon}}_p = \dot{\lambda}_p \frac{\partial f_p(\boldsymbol{\sigma})}{\partial \boldsymbol{\sigma}}, \qquad \dot{\lambda}_p \geq 0 \tag{4.04}$$

However, the *non-associative* plasticity is implemented in the non-linear cementitious model. In such a case, it is *not associated* with a plasticity function but with a plastic potential function g_P and $\mathbf{g}_P(\boldsymbol{\sigma})$ is its gradient

$$\dot{\boldsymbol{\varepsilon}}_p = \dot{\lambda}_p \frac{\partial g_p(\boldsymbol{\sigma})}{\partial \boldsymbol{\sigma}}, \qquad \dot{\lambda}_p \geq 0 \tag{4.05}$$

The plastic potential function can have a similar shape as the plasticity function, but some parameters are changed making the plastic strain description more realistic [23].

Following the unified theory of an elastic degradation, it is possible to define analogous quantities for the fracturing model $\dot{\boldsymbol{\varepsilon}}_f$

$$\dot{\boldsymbol{\varepsilon}}_f = \dot{\lambda}_f \mathbf{g}_f(\boldsymbol{\sigma}), \qquad \dot{\lambda}_f \geq 0, \qquad \mathbf{g}_f(\boldsymbol{\sigma}) = \frac{\partial g_f(\boldsymbol{\sigma})}{\partial \boldsymbol{\sigma}} \tag{4.06}$$

where $\dot{\boldsymbol{\varepsilon}}_f$ is the fracture strain rate, $\dot{\lambda}_f$ is the inelastic fracturing multiplier and $\mathbf{g}_f(\boldsymbol{\sigma})$ is the potential, defining the direction of inelastic fracturing strains in the fracturing model.

4.1.2 Fracture Model

The Rankine criterion is used for concrete cracking. A visualization of the Rankine criterion in Westergaard coordinates appears in the Figure 4.1.

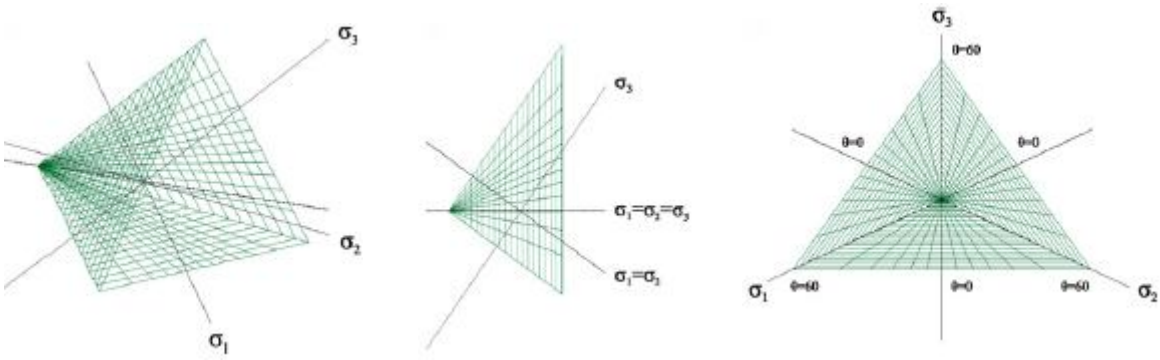

(a) 3D stress space *(b) Rendulić plane* *(c) deviatoric plane*

Fig. 4.1: Rankine failure surface in Westergaard coordinates [21]

An interesting property of the Rankine criterion is that it reaches infinite values for compression. It means that if loaded by compression, plastic deformation never occurs and the behavior stays elastic for an arbitrarily big loading.

The crack opening w is computed from the total accumulated value of strain $\hat{\boldsymbol{\varepsilon}}_f$ in a direction k [4], plus the current increment of fracturing strain, and this sum is multiplied by the characteristic length L_t. The characteristic length is actually a crack band size. In this model, the crack band size is calculated as a width or size of the element projected into the direction k. This is illustrated in Figure 4.2. It has been proven that this approach is satisfactory for linear finite elements. The crack band approach assures that the energy dissipation is not too sensitive with respect to the finite element size.

[4] In the case of rotated crack model, the direction k corresponds to the instantaneous principal strain directions. However, in the case of fixed crack model, it is given by the principal strain directions at the onset of the cracking.

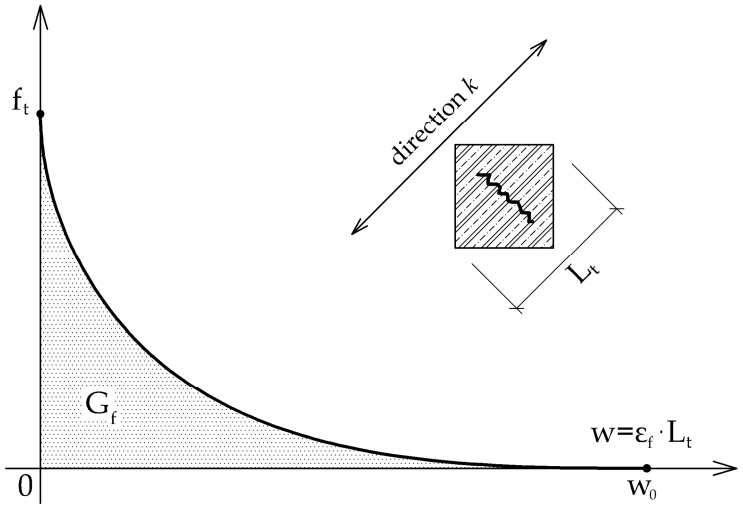

Fig. 4.2: Tensile strength function with respect to crack width

It is important to distinguish between total fracturing strain $\hat{\varepsilon}_f$, which corresponds to the maximum fracturing strain at material direction *k* reached during the loading process, and the current fracturing strain ε_f, which can be smaller due to crack closure.

The area below the graph in Figure 4.2 equals to a material property called fracture energy G_f. It is energy (or work) needed for exceeding of the material cohesion. This energy depends on the type of material and on the area of a new crack, therefore the unit is $Jm^{-2} = Nm^{-1}$.

4.1.3 Plasticity Model

In this model, the Menétrey and Willam three parameter failure surface is used. A visualization of the Menétrey and Willam criterion in Westergaard coordinates is shown in the Figure 4.3.

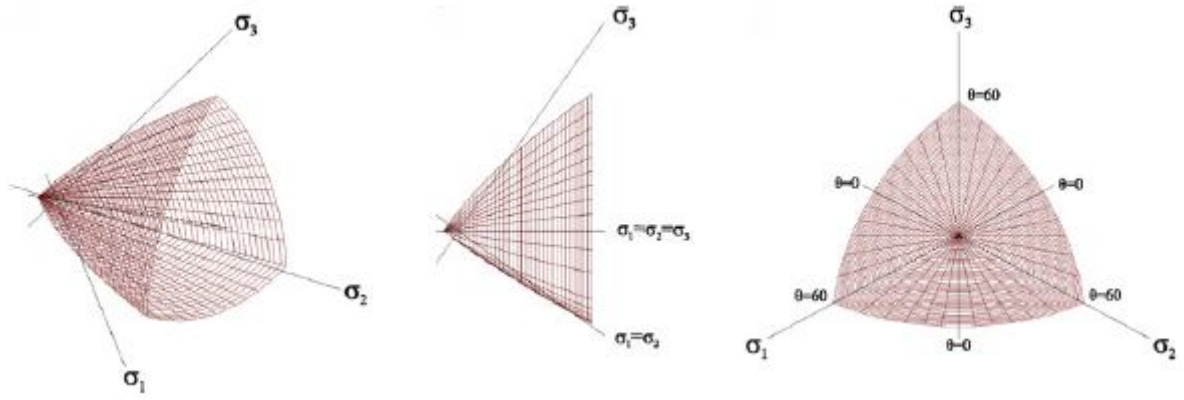

(a) 3D stress space *(b) Rendulić plane* *(c) deviatoric plane*

Fig. 4.3: Menétrey-Willam failure surface in Westergaard coordinates [21]

Very important parameter in the model is λ_t, which must be bigger or equal to 1. It scales value for the tensile concrete strength in order to provide intersection between the Rankine (fracture) and the Menétrey-Willam (plasticity) failure surfaces during the combination procedure, as it is shown in Figure 4.4. Then the parameter $e \in (0,5;1,0)$ defines the roundness of the Menétrey-Willam failure surface, with a recommended value $e = 0,52$ leading to biaxial concrete strength equal to $f_{bc} = 1,14f_c$. The failure surface has sharp corners if $e = 0,5$, and is fully circular around the hydrostatic axis if $e = 1,0$.

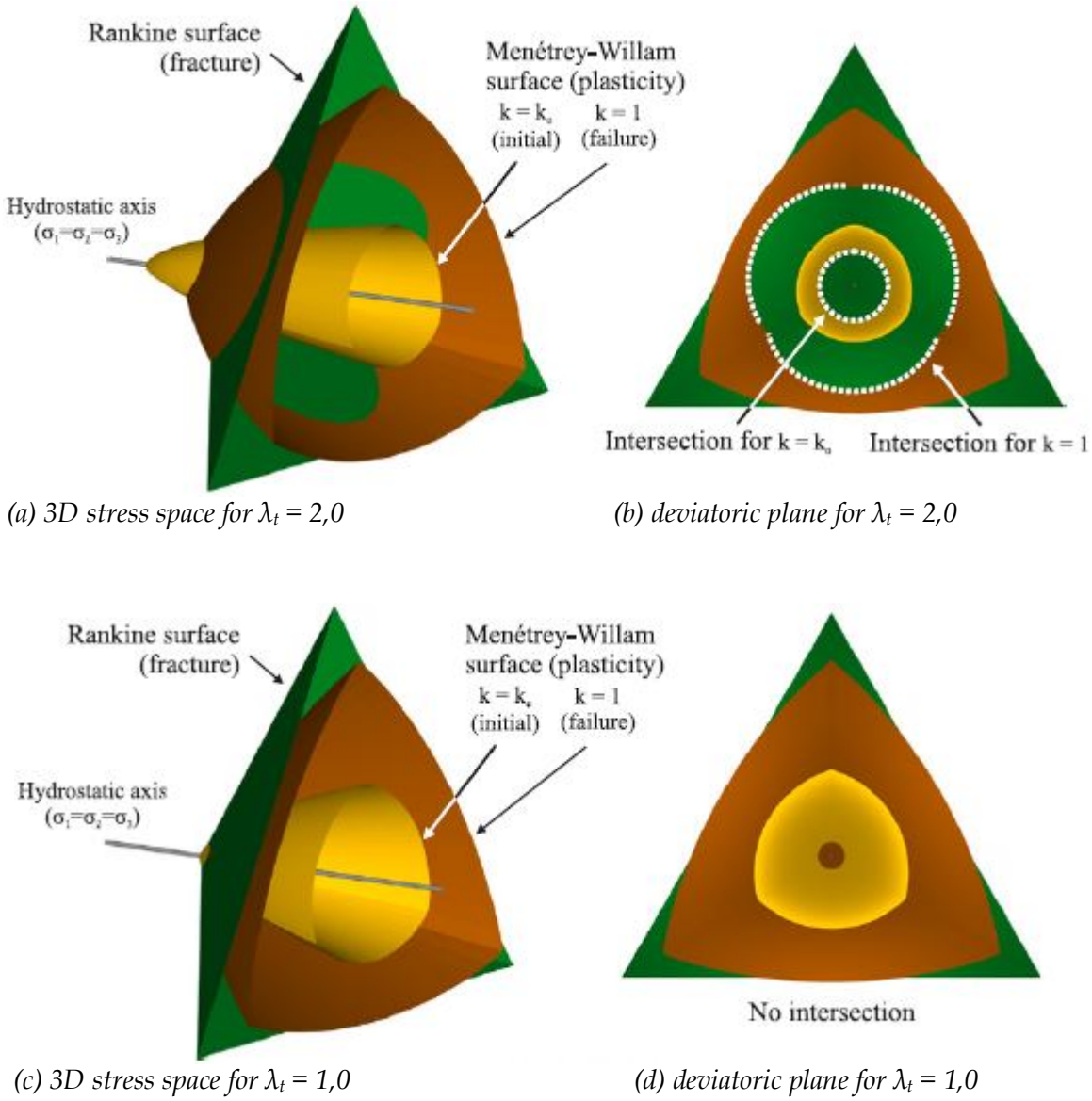

(a) 3D stress space for $\lambda_t = 2,0$ *(b) deviatoric plane for $\lambda_t = 2,0$*

(c) 3D stress space for $\lambda_t = 1,0$ *(d) deviatoric plane for $\lambda_t = 1,0$*

Fig. 4.4: Rankine and Menétrey-Willam failure surfaces put together for different λ_t [21]

The position of the Menétrey-Willam failure surface is not fixed but it can expand and move along the hydrostatic axis (simulating hardening and softening stages),

based on the value of the hardening/softening parameter κ. In the model, this parameter indentifies with the volumetric strain

The instantaneous shape and location of the loading surface during hardening is defined by a hardening function k, which depends on the hardening/softening parameter κ. This function is directly incorporated in the Menétrey-Willam failure surface and it has two main parameters. $\varepsilon_p^{v,t}$ is the plastic volumetric strain at uniaxial concrete strength (onset of softening) and k_o is the value that defines the initial yield surface that bounds the initial elastic regime (onset of plasticity).

At the end of the hardening process, the hardening function retains a constant value of unity and the material enters the softening regime, which is controlled by softening function c. This function simulates the material decohesion by shifting the loading surface along the negative hydrostatic axis. The softening function value starts from unity and complete material decohesion is attained at $c = 0$. The evolution of both, hardening and softening functions with respect to the hardening/softening parameter is schematically shown in Figure 4.5.

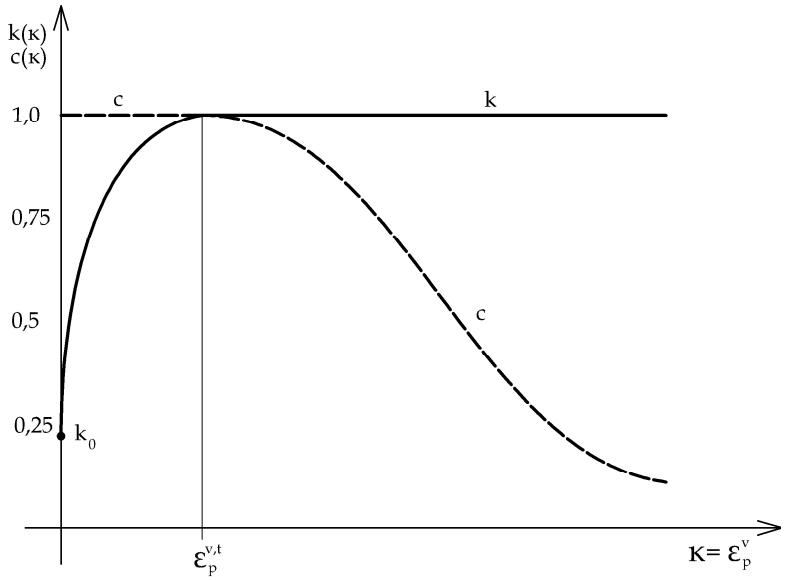

Fig. 4.5: Hardening and softening functions with respect to plastic volumetric strain

Another important parameter is a direction of the plastic flow β. If $\beta<0$ material is compacted during crushing, if $\beta = 0$ material volume is preserved, and if $\beta>0$ material is dilated [24].

4.2 Solution of Non-Linear Equations

In the previous Section 4.1, there were described all the parameters that can be set in a *New material* menu in the ATENA program, if one of the 3D non-linear cementitious material models is chosen (there are four of them, each offering different setting possibilities).

This section is dedicated to the solution of non-linear equations. In general, these can be solved either by direct solvers or by iterative solvers. However, all of them have one common problem – necessity to solve a set of linear algebraic equations.

The direct solvers have given number of steps and operations, which must be done, in advance. The Gauss elimination based algorithms makes the solution slow and demanding with respect to a memory of a computer whereas sparse solvers are stable a reliable, are less demanding on a memory of a computer, and are faster then the Gauss elimination [25].

The iterative solvers are suitable for solution of big problems, when the memory is not big enough for the sparse solver. The approximate solution of the set of equations is searched iteratively in such a way that the norm of the difference between the right hand side (internal forces) and the left hand side (external forces) of the equation must be smaller than a given tolerance [25].

Hereinafter, there are mentioned several methods which are implemented in ATENA.

4.2.1 Full Newton-Raphson Method

This method is very good for a demonstration of the iterative procedure. Using the concept of incremental step-by-step analysis, we obtain the following set of non-linear equations

$$\mathbf{K}(\mathbf{d})\,\Delta\mathbf{d} = \mathbf{f}_{ext} - \mathbf{f}_{int}(\mathbf{d}) \tag{4.07}$$

where $\mathbf{f}_{ext}$ is the vector of total equivalent nodal loads, $\mathbf{f}_{int}(\mathbf{d})$ is the vector of internal joint forces, $\Delta\mathbf{d}$ is the displacement increment due to loading increment, $\mathbf{d}$ are the displacements of structure before load increment and $\mathbf{K}(\mathbf{d})$ is the stiffness matrix, relating loading increments to displacement increments.

The right hand side of the equation (4.07) represents out-of-balance forces during a load increment, i.e. the total load level after applying the loading increment minus forces at the end of the previous load step. Generally, the stiffness matrix is displacement dependent, it is a function of $\mathbf{d}$, but this is usually neglected within a load increment in order to preserve linearity. In this case, the stiffness matrix is calculated based on the value of $\mathbf{d}$ related to the level before the load increment [24].

The non-linearity of the equation (4.07) can be shown on the non-linearity of the internal forces, because

$$\mathbf{f}_{int}(k\,\mathbf{d}) \neq k\,\mathbf{f}_{int}(\mathbf{d}) \tag{4.08}$$

where k is an arbitrary constant, and the non-linearity can be also illustrated on the stiffness matrix, because

$$\mathbf{K}(\mathbf{d}) \neq \mathbf{K}(\mathbf{d} + \Delta\mathbf{d}) \tag{4.09}$$

The set of equations represents the mathematical description of structural behavior during one step of the solution. Rewriting equations (4.07) for the *i-th* iteration, we get

$$\mathbf{K}(\mathbf{d}_{i-1})\,\Delta\mathbf{d}_i = \mathbf{f}_{ext} - \mathbf{f}_{int}(\mathbf{d}_{i-1}) \tag{4.10}$$

All the quantities for the *(i-1)th* iteration have already been calculated during the previous solution steps. Now we solve for $\mathbf{d}_i$ at load level $\mathbf{f}_{ext}$ using

$$\mathbf{d}_i = \mathbf{d}_{i-1} + \Delta\mathbf{d}_i \tag{4.11}$$

The concept of the solution by full Newton-Raphson method (NRM) is illustrated in Figure 4.6.

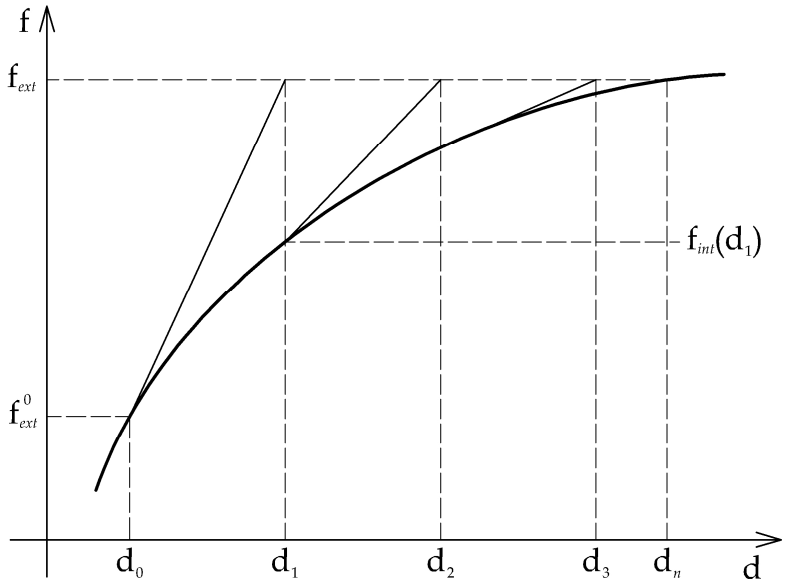

Fig. 4.6: Full Newton-Raphson method

As explained above, the equation (4.10) is non-linear and therefore it is necessary to iterate until some convergence criterion is satisfied. The following possibilities are supported in ATENA [24]

$$\frac{\left\|\Delta\mathbf{d}_i\right\|_2}{\left\|\mathbf{d}_i\right\|_2} \leq \varepsilon_D \tag{4.12}$$

This criterion checks the norm of displacement changes. It says that the norm of the displacement increment vector must be small enough when compared with the norm of the total displacement vector at the end of iteration. Although this convergence criterion is effective in the analysis of a one-degree-of-freedom system, experience has shown that in general, non-linear analysis the convergence factor can be ill-behaved[5] and therefore it is not a reliable indicator of how the iteration is proceeding [26].

A more reliable convergence criterion is based on the out-of-balance forces. A force convergence criterion requires that the norm of the out-of-balance load vector be within a preset tolerance ε_F of the original load increment

$$\frac{\left\|\mathbf{f}_{ext} - \mathbf{f}_{int}(\mathbf{d}_{i-1})\right\|_2}{\left\|\mathbf{f}_{int}(\mathbf{d}_i)\right\|_2} \leq \varepsilon_F \tag{4.13}$$

The major disadvantages in using a force check are that inconsistencies in units can appear in the force vector (e.g. forces and moments in beam elements) and that the displacement solution does not enter the termination criterion [26].

In order to provide some indication of when both the displacements and forces are near their equilibrium values, the increment in internal energy during each iteration (i.e. the amount of work done by the out-of-balance loads on the displacement increments) can be compared to the initial internal energy increment. Convergence is assumed to be reached when [26]

$$\frac{\left\|\Delta\mathbf{d}_i^T \left(\mathbf{f}_{ext} - \mathbf{f}_{int}(\mathbf{d}_{i-1})\right)\right\|_2}{\left\|\mathbf{d}_i^T \mathbf{f}_{int}(\mathbf{d}_i)\right\|_2} \leq \varepsilon_E \tag{4.14}$$

The various characteristics of termination criteria make it difficult to recommend a check for all nonlinear analyses. However, it appears that a combination of force and energy checks (equations (4.13) and (4.14)) provide the most effective convergence criteria because increments in both terms tend to zero near the solution, and together they provide some measure of the accuracy of both displacements and forces. Also, the energy check (equation (4.14)) with ε_E = 1 is recommended as a check for divergence [26].

However, the ATENA contains one more check of out-of-balance forces in terms of maximum components, rather than Euclidian norms

$$\frac{\left\|\max\left(\mathbf{f}_{ext}^k - \mathbf{f}_{int}^k(\mathbf{d}_{i-1})\right)\right\|_2}{\left\|\max\left(\mathbf{f}_{int}^k(\mathbf{d}_i)\right)\right\|_2} \leq \varepsilon_{MF} \tag{4.15}$$

All the convergence limits ε are set by default to 0,01 (i.e. 1%).

[5] Said of an algorithm or computational method that tends to blow up because of accumulated round off error or poor convergence properties.

4.2.2 Modified Newton-Raphson Method

This method is not among the default options in ATENA, but it can be very easily set, by modifying the full NRM. A reason for the modification is that the most time consuming part of solution of equation (4.10) is the recalculation of the stiffness matrix $\mathbf{K}(\mathbf{d}_{i-1})$ at each iteration. In many cases this is not necessary and we can use matrix $\mathbf{K}(\mathbf{d}_0)$ from the first iteration of the step. This is the basic idea of the modified NRM. It produces very significant time saving, but on the other hand, it also exhibits worse convergence of the solution procedure.

The simplification adopted in the MNRM can be mathematically expressed as

$$\mathbf{K}(\mathbf{d}_{i-1}) \approx \mathbf{K}(\mathbf{d}_0) \tag{4.16}$$

This method is depicted in Figure 4.7. By simple comparing Figures 4.6 and 4.7, it is clear that the MNRM converges more slowly than the full NRM. On the other hand, a single iteration costs less computing time, because it is necessary to assemble and eliminate the stiffness matrix only once. In practice, a careful balance of the two methods is usually adopted in order to produce the best performance for a particular case. Usually, it is recommended to start a solution with the original Newton-Raphson method and later, it means near extreme points, switch to the modified procedure to avoid divergence [24].

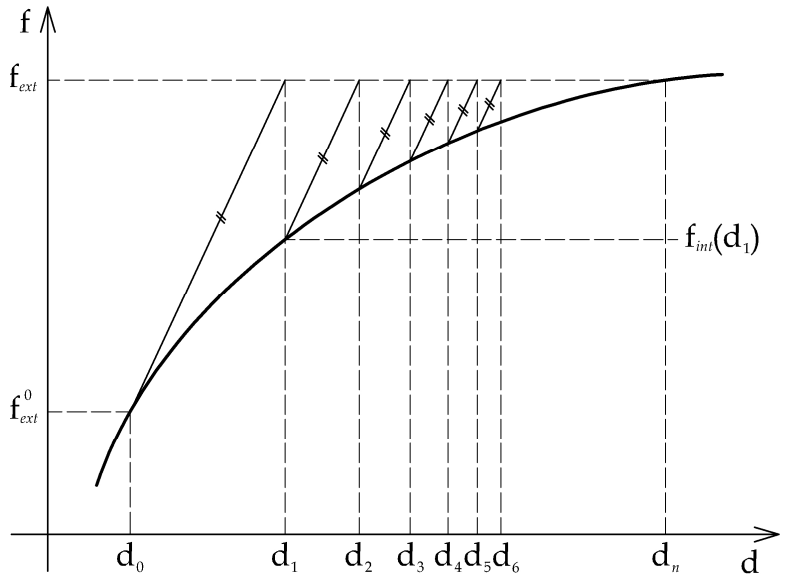

Fig. 4.7: Modified Newton-Raphson method

4.2.3 Arc-Length Method

Load controlled NRM fails near the limit point. To overcome difficulties with limit points, displacement control techniques were introduced. However, for structural systems exhibiting snap-through or snap-back behavior, even these techniques lead

to error. Several ways to overcome the problem are to switch between load and displacement controls, use the artificial springs, or abandon the equilibrium iterations in the close vicinity of the limit point.

To obtain a more general technique, the arc-length method, originally developed by Riks (1972; 1979) and Wempner (1971) and later modified by several scholars, is used. Because of its good performance, it is now quite well established for geometric non-linearity and for material non-linearity as well.

The primary task is to observe complete load-displacement relationship rather then applying a constant loading increment, as it is in the Newton-Raphson method. Hence, this method fixes not only the loading but also the displacement conditions at the end of a step. There are many ways of fixing these, but one of the most common is to establish the length of the loading vector and displacement changes within the step.

From the mathematical point of view it means that we must introduce an additional degree of freedom associated with the loading level (i.e. a problem has n displacement degrees of freedom and *one* for loading) and in addition, a constraint for the new unknown variable must be introduced. The new degree of freedom is usually named λ. The basic equation can be rewritten from the equation (4.07) as

$$\mathbf{K}(\mathbf{d})\,\Delta\mathbf{d} = \lambda\mathbf{f}_{ext} - \mathbf{f}_{int}(\mathbf{d}) \tag{4.17}$$

where λ is the new loading factor and the vector $\mathbf{f}_{ext}$ is not, in this case, the total loading at the end of the step, but it is only a reference loading type, which is scaled by the λ. The stiffness matrix $\mathbf{K}(\mathbf{d})$ can be either recomputed for every iteration (similar to full NRM) or it can be fixed based on the first iteration for all subsequent iterations (similar to MNRM).

There are many possibilities for defining constraints on λ and those implemented in ATENA are:

- Crisfield method
- Normal update method
- Consistently linearized method
- Explicit orthogonal method

For more details about these methods, see ATENA Program Documentation [24].

4.2.4 Line Search Method

Generally, this optimization method is based on the variational principle, which determines the solution of a set of equations in a form of **Ax=b**. It says that if **A** is positive definite, then the energy which the functional attains is a unique minimum; this minimum occurs at the solution of **Ax=b**. To reach the minimum, we need to know a step length and a descent direction, in which the minimum is approached. Once a descent direction is known, the problem of computing an appropriate step

length is reduced to finding the minimum of a function of a single variable. This process is known as a *line search*.

In ATENA, the objective of this method is to calculate the parameter η. The scalar η is used to accelerate solutions in cases of well-behaved load-deformation relationships or to damp possible oscillations, if some convergence problems arose, e.g. near bifurcation and extreme points.

The basic idea behind η is to minimize work of current out-of-balance forces on displacement increment. The line search method can be used with both, Newton-Raphson method and arc-length method.

Simply, we can use any method to calculate displacement increment $\boldsymbol{\delta}$, then we calculate vectors of out-of-balance forces $\mathbf{g}(\mathbf{d}_{i-1})$ and $\mathbf{g}(\mathbf{d}_{i-1}+\eta_{i-1}\cdot\boldsymbol{\delta}_{i-1})$, and finally, we calculate parameter η. Since the equations are non-linear, the scalar η must be solved by iterations until the ratio of norms of the vectors of out-of-balance forces is not less or equal to a specified energy drop, typically in the range from 0,6 to 0,8 [19].

5 Numerical Simulations

Originally, the plan was to use a paper by Baronio, Binda, Lombardini (1997) [13], which has already served as a source for mixing ratios of mortar samples prepared in a laboratory and there is also presented an experiment of a masonry structure with thick joints. The experiment should have been repeated by a numerical simulation and the parameters used in ATENA then fitted to results of the real experiment. However, after thorough study it was found useless, because they use fresh mortar. It is obvious that the monitored displacements were huge even without an external loading and stresses the structure was able to withstand were very small.

Because the cocciopesto is not a usual type of mortar, it was not possible to find another experiment dealing with cocciopesto, which would be suitable for comparison and fitting of results. Therefore, a new research of a literature began, in order to find a suitable type of experiment settings, no matter what mortar was used.

Since the extraordinary earthquake resistance is attributed to the thick joints made of the cocciopesto mortar (see Section 1.4), structures subjected to shear were of the main interest. Finally, after a comparison of several papers dealing with the issue of shear walls and pushover analyses, a final setting was chosen.

5.1 Numerical Model

It is a masonry wall with fixed foot and the top of the wall has enabled rotations and horizontal displacements only. Self-weight is not taken into account. There is a steel plate placed on the top, to distribute the stresses caused by a prescribed displacement $\bar{u}$ in x-direction. This simulates a laboratory setting with restricted push-over mode, when the tested walls are placed into a steel frame with hydraulic jacks. There were monitored two quantities. Number one is load monitored just next

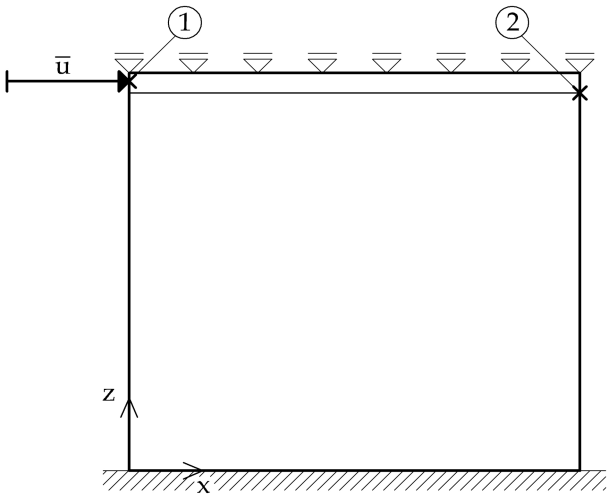

Fig. 5.1: Shear wall scheme

to the applied displacement and number two is displacement monitored in the right top corner of the wall. It is schematically illustrated in Figure 5.1.

It was planned to compare a response of structures with cocciopesto mortar and "standard" mortar. Nevertheless, to find all necessary mechanical properties of the standard mortar in one paper turned out to be impossible and find them in several papers is very disputable, because the individual mortars evaluated in different papers and laboratories are always different as well, depending very strongly on mix ratios, setting and hardening conditions, curing time etc. Therefore, such a procedure of obtaining mechanical properties would result in hybrid mortar with unreasonable characteristics. The sound method of comparing two mortars is to get own results from own testing. Unfortunately, our own samples of the cocciopesto mortar are still in moulds and not ready for testing, as you can see in Figure 5.2.

Fig. 5.2: Samples of cocciopesto mortar in laboratory

From the reasons stated above, the strategy was changed from comparing two mortars, to comparing one mortar with various mechanical properties and used on different types of walls, while observing trends rather than absolute peak or collapse values.

5.2 Setting of ATENA

There were carried out both analyses, 2D and 3D. 2D pre-processing was done in ATENA 2D version 3.2.0.0, while analysis and post-processing were done in ATENA 2D version 4.2.2.0. In a case of 3D, the pre-processing was done in ATENA 3D version 3.2.0 and analysis with post-processing in ATENA 3D version 4.2.5.3252.

5.2.1 Materials

There were used two different material models and three materials. Material model 3D nonlinear cementitious 2 was used for both, the cocciopesto mortar and the clay bricks in 2D and 3D analyses. All the material parameters, which are possible to set for the cocciopesto mortar, are shown in Table 5.1. Only the parameters E, μ, f_c and f_t were set different from default values. It was done according to preliminary results of micromechanical homogenization by Nežerka (2011) [27].

Table 5.1: Material parameters of cocciopesto mortar

Elastic modulus E [MPa]:	2200	Fail. surface eccentricity e [-]:	0,52
Poisson's ratio μ [-]:	0,202	Specific material weight ρ [kgm^{-3}]:	2300
Tensile strength f_t [MPa]:	0,7	Plastic strain at compressive strength ε_{cp} [-]:	-3,489E-4
Compressive strength f_c [MPa]:	-5,0	Coefficient of thermal expansion α [K^{-1}]:	1,2E-5
Specific fracture energy G_f [Nm^{-1}]:	19,55	Fixed crack model coefficient [-]:	1,0
Critical compressive displacement w_d [mm]:	-0,5	Multiplier for plastic flow direction β [-]:	0,0

The parameters for the clay brick appear in Table 5.2. Again, only the parameters E, μ, f_c and f_t were changed. These were taken from paper by Brencich et al. [28].

Table 5.2: Material parameters of clay brick

Elastic modulus E [MPa]:	2400	Fail. surface eccentricity e [-]:	0,52
Poisson's ratio μ [-]:	0,2	Specific material weight ρ [kgm^{-3}]:	2300
Tensile strength f_t [MPa]:	3,4	Plastic strain at compressive strength ε_{cp} [-]:	-7,045E-4
Compressive strength f_c [MPa]:	-18,7	Coefficient of thermal expansion α [K^{-1}]:	1,2E-5
Specific fracture energy G_f [Nm^{-1}]:	47,11	Fixed crack model coefficient [-]:	1,0
Critical compressive displacement w_d [mm]:	-0,5	Multiplier for plastic flow direction β [-]:	0,0

For the steel plate on the top of the wall, plane stress elastic isotropic material model was used for 2D analysis and 3D elastic isotropic for 3D analysis respectively. All material parameters, which are possible to change, are shown in Table 5.3 and all of them were left as they were set by default.

Table 5.3: Material parameters of steel plate

Elastic modulus E [GPa]:	210	Specific material weight ρ [kgm^{-3}]:	2300
Poisson's ratio μ [-]:	0,3	Coefficient of thermal expansion α [K^{-1}]:	1,2E-5

5.2.2 Solution Parameters

The objective is to trace the load-displacement curve up to the post-failure softening regime. It would be possible to prescribe loading in terms of forces and use the arc-length method, which automatically changes the sign of load increment once a peak is attained. Alternatively, displacement can be prescribed. Since displacement will keep on increasing even after the wall fails, either the Newton-Raphson method or arc-length method can be employed. Due to its better stability, the Newton-Raphson solution method was chosen.

To speed up convergence of the solution, the full Newton-Raphson method with tangent stiffness updated in each iteration was employed. To automatically adjust the speed of analysis according to the non-linearity of the response, the line search method was utilized. All the parameters are summarized in Table 5.4.

Table 5.4: Summary of solution parameters

Solution method:	Newton-Raphson
Update stiffness:	Each iteration
Stiffness type:	Tangent
Iteration limit for step:	40
Error tolerances:	0,01
Line search:	on, with iterations

However, before the solution method was finally decided, comparison of the Newton-Raphson method and arc-length method was done, in order to be sure that the methods do not differ significantly in any phase of the loading. Because then it would be necessary to find the reason of the difference and maybe even to change the solution method. A graph showing the results of both methods is in Figure 5.3. As you can see, both methods are perfectly corresponding up to the peak and even in

post-peak phase the correspondence is almost perfect. Since the NRM was less time demanding, the above made choice was just approved by this comparison.

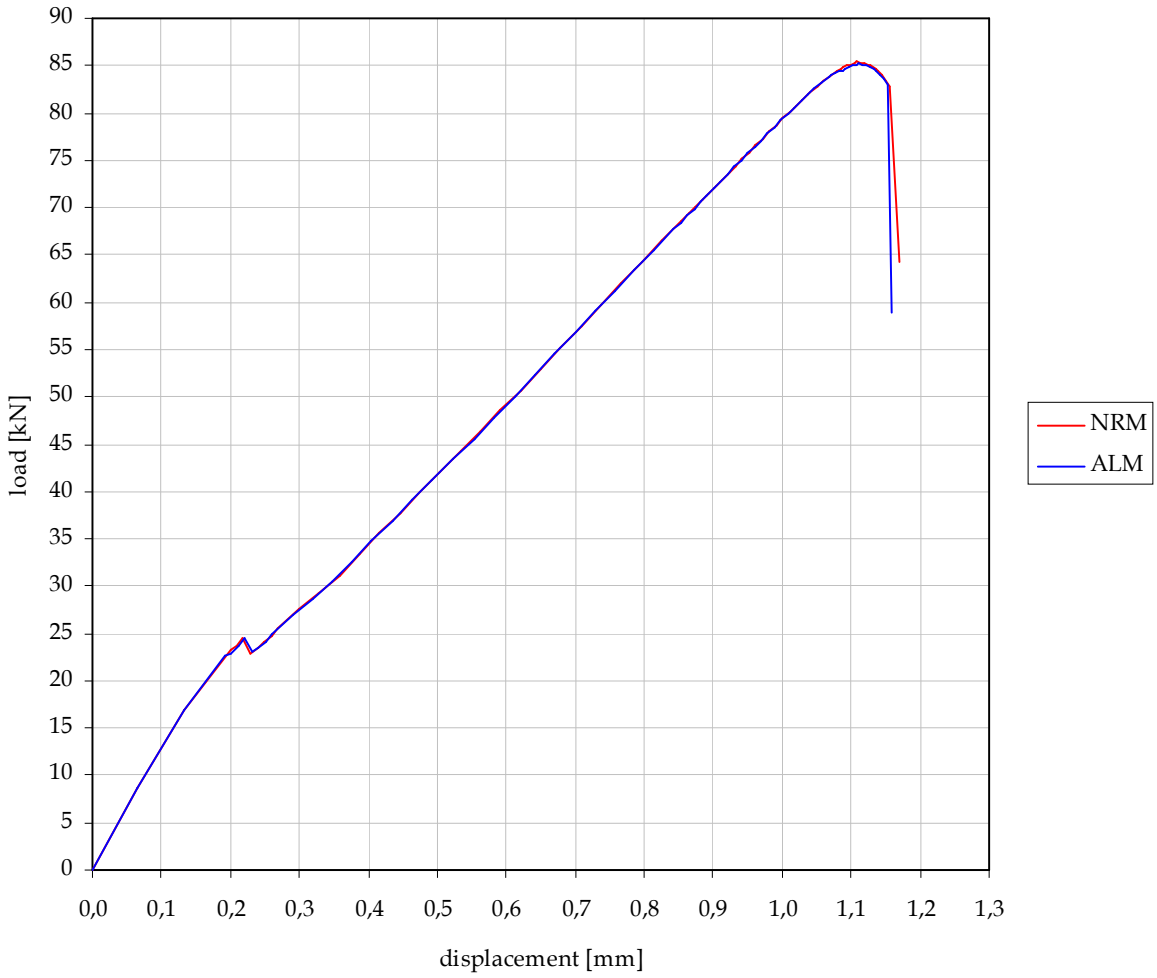

Fig. 5.3: Newton-Raphson method vs. Arc-length method

As mentioned in Section 4.2.3, for large or brittle beams, a snap-back behavior may occur, in which case both displacement and force increments change their sign upon failure. In such situation, the arc-length solution would be the only applicable method.

5.2.3 Meshing

The quadrilateral elements in 2D and the brick elements in 3D analyses were used, wherever it was possible. Since the wall was modeled as bricks and mortar joints separately, without any homogenization, the size of the elements varied from case to case.

To know the importance of a fineness of meshing on the solution, comparative analyses were carried out. The result is depicted in Figure 5.4. It is apparent that the curves are different in values but not so much different in shapes. As it was

discussed in Section 3.2, FEM is based on minimum potential energy theorem and therefore it converges to the correct solution from a higher value as the number of elements in the model increases. Therefore, it is clear that the finer meshing gives more precise results.

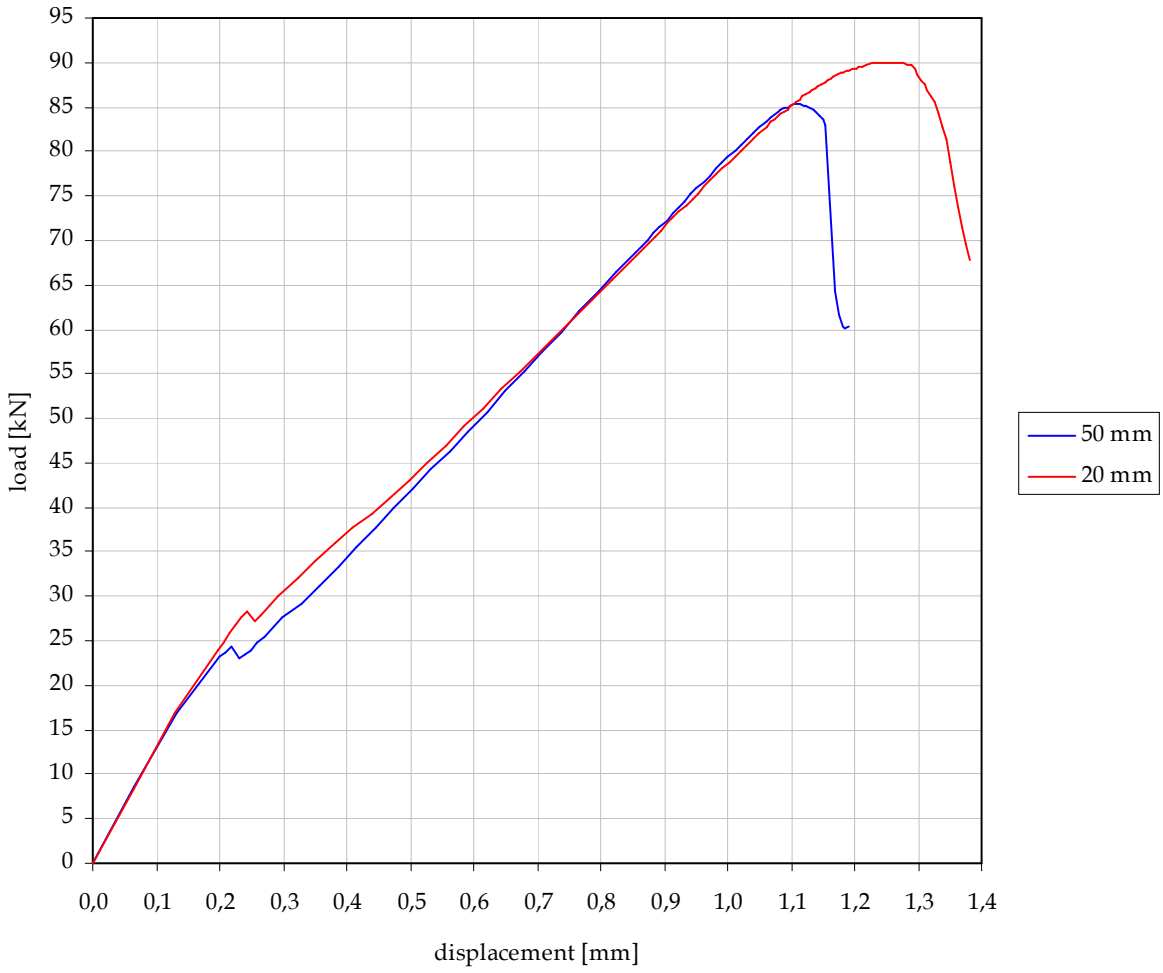

Fig. 5.4: Influence of fineness of meshing

However, the finer meshing was extremely demanding on a computer and time. Executing more such analyses would have been unfeasible. In addition, as mentioned in Section 5.1, the aim is to observe trends rather than precise peak or collapse values. From these reasons, the absolute accuracy of the results is not essential and the less fine meshing was chosen for further analyses.

5.2.4 2D analysis vs. 3D analysis

Another important decision was, whether use 2D or 3D analysis. It is obvious that 2D analysis needs fewer elements and therefore it is much more time efficient than 3D analysis. Nevertheless, before the 2D analysis was adopted for its advantages, it was necessary to check a correspondence of these two analyses. For this comparison,

a standard wall with 10 mm thick joints was chosen. The concrete dimensions of the wall and bricks will be discussed in the following sections. A graphical result of the comparison is shown in Figure 5.5. Apparently, in this case not only values differ, but also the shapes are quite different, especially in the peak zone. Generally, the 3D analysis is usually more realistic, but it was necessary to prove that this is also the case.

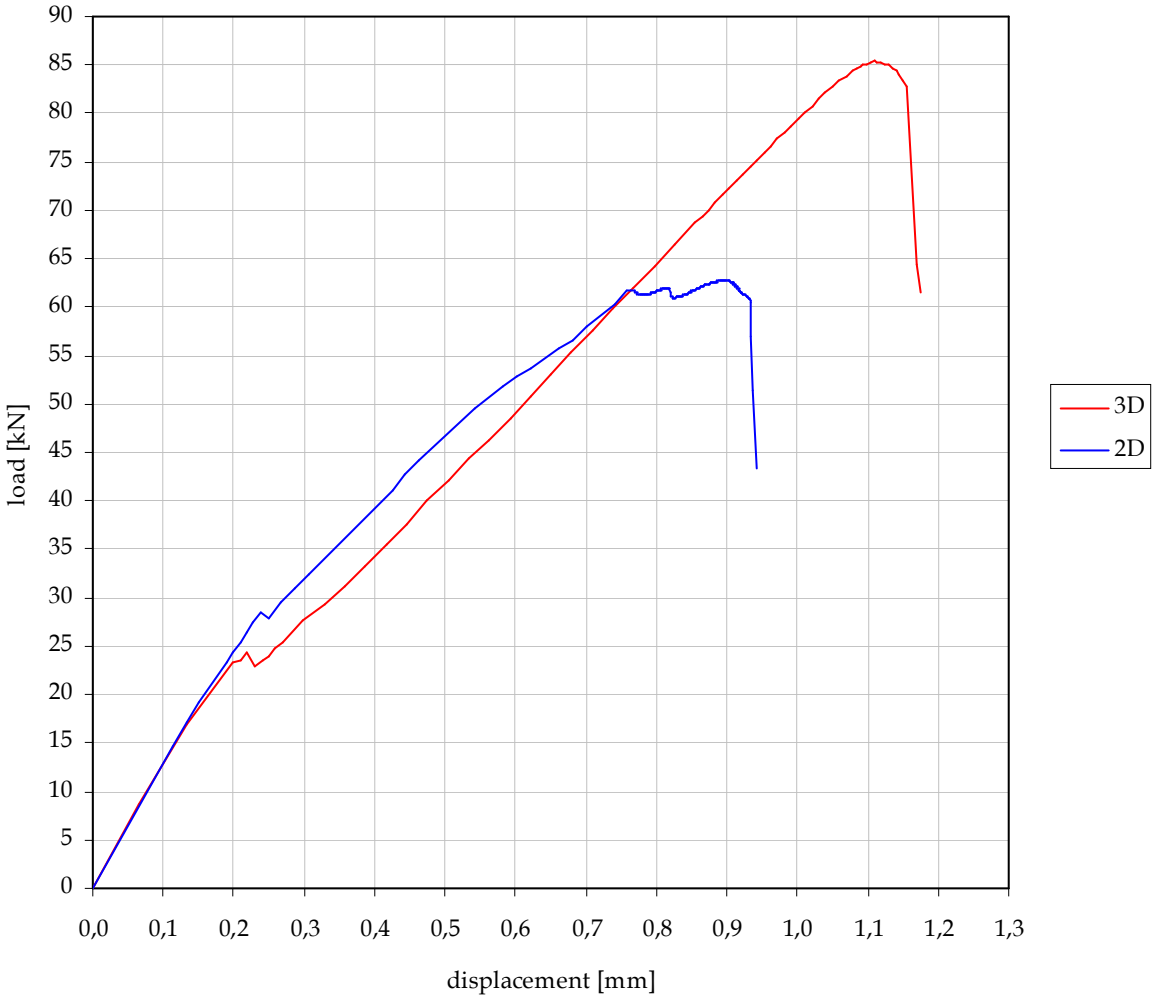

Fig. 5.5: 2Danalysis vs. 3D analysis

Pictures of the cracked walls were very helpful in this issue. As you can see in Figures 5.6 and 5.7, the distribution of cracks is in both cases very different. One would have naturally expected a crack pattern similar to Figure 5.7, especially when taking into account the direction of maximum principal stress, respectively the direction of the tensile diagonal. Moreover, when this assumption was supported by Figure 5.8 from an experiment made by Maheri et al. (2008) [29], there were no doubts that the 3D analysis really gives more reasonable and realistic results. Therefore, all the following analyses are performed in 3D.

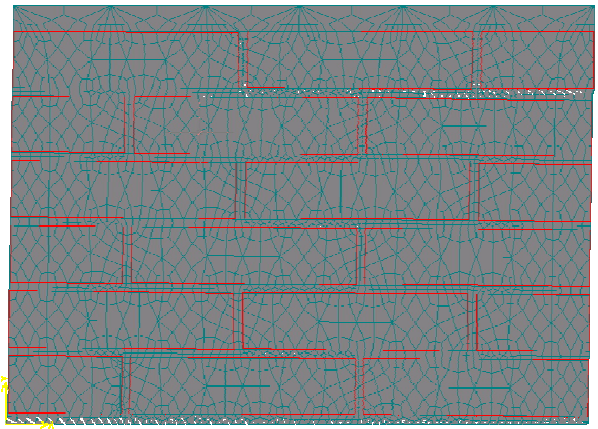

Fig. 5.6: Crack pattern of 2D shear wall

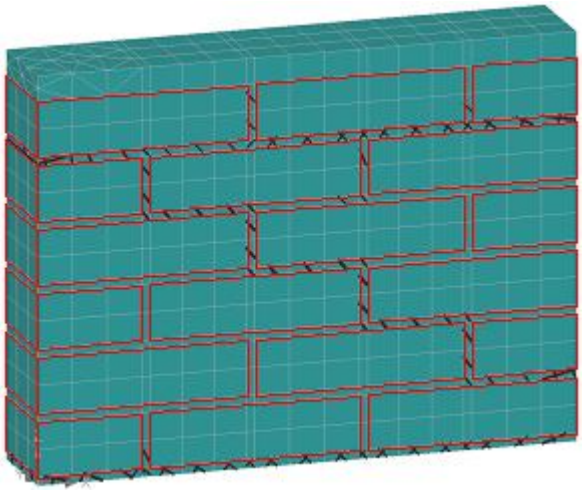

Fig. 5.7: Crack pattern of 3D shear wall

Fig. 5.8: Crack pattern of experimental shear wall [29]

5.3 Influence of Geometry

In this section, an influence of different wall geometries on a structural behavior is examined.

There are used the clay bricks with properties described in Section 5.2.1 and they are so-called small format full bricks with dimensions 250 x 120 x 65 mm. The same or similar type of bricks was used in several papers, e.g. Brasile et al. (2007) [6] or Brencich et al. [28]. This type of bricks was used in all analyses in this thesis and there are always six rows of the bricks, with two and half brick in each row.

The properties of the used cocciopesto mortar are described in Section 5.2.1 and they do not change throughout the current section.

5.3.1 Thickness of Joints

To find out the influence of the thickness of the joints is very interesting task. It was investigated on two different walls.

The first wall has standard 10 mm thick cocciopesto mortar joints. The geometry of this wall, with all important dimensions, is depicted in Figure 5.9.

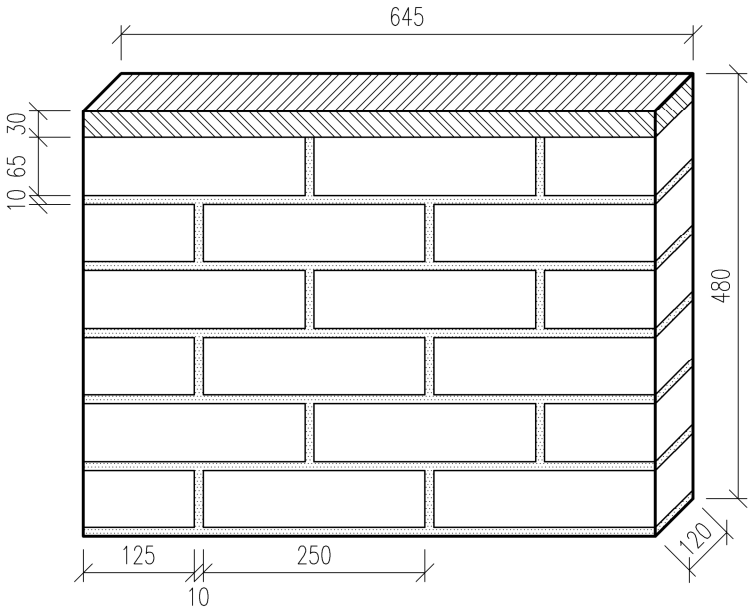

Fig. 5.9: Shear wall with 10 mm thick joints

The second wall has 45 thick joints, made of cocciopesto mortar. This thickness was chosen according to Baronio, Binda, Lombardini (1997) [13], who studied the coociopesto mortar coming from the remaining of the original walls of St. Michele in Africisco. The geometry and dimension are shown in Figure 5.10. The wall may seem little bit ridiculous, in comparison with the first wall. However, you can see that the thickness of the bricks is still bigger than thickness of the joints, and as you know

from Section 1.1, it was no exception in ancient times, if the joints were even thicker than the bricks.

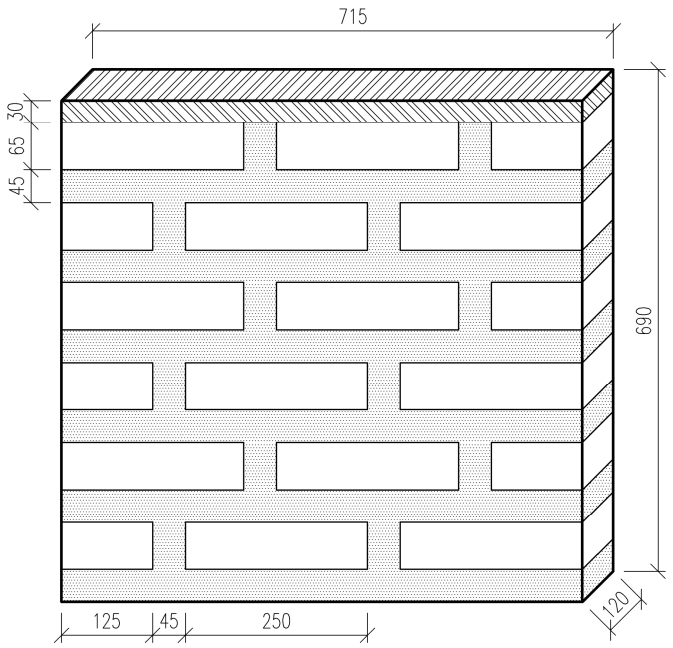

Fig. 5.10: Shear wall with 45 mm thick joints

Both walls were subjected to the same prescribed displacements and deformed a little beyond the peak values. Again, this loading procedure was done in all performed analyses. The load-displacement graphs of both analyses are depicted in Figure 5.11 and coordinates of peak values are in Table 5.5.

Table 5.5: Summary of peak values for different thicknesses of joints

Thickness of joints [mm]	Displacement [mm]	Load [kN]
10	1,11	85,38
45	1,74	83,85

We can observe several interesting fact in the graphs. For example, note the small discontinuities of the curves, around the loading of 20 kN. These are caused by a sudden propagation of cracks in the right top horizontal joint, because the joint tries to "open", as the right top corner of the wall is being pushed aside.

Another interesting fact is that the wall with 45 mm thick joints is apparently more compliant than the wall with 10 mm thick joints, but practically without any loss of resistance. This is rather remarkable. This is due to a bigger content of the "weak"

member, i.e. mortar, in the wall, which makes the wall with 45 mm thick joints less stiff. The higher compliance is advantageous in situations, when e.g. differential settlement or other non-force loading can occur. Most importantly, the compliant structures are also able to resist dynamic effects in a bigger extent than the stiff ones. This can be one of the reasons, why the ancient structures with thick joints were able to withstand a high seismicity for many hundreds of years, as for example Hagia Sofia in Istanbul.

You have also probably noticed the shape difference of the peak zones of both walls. It is smooth in the case of the 10 mm thick joints and very sharp in the case of the 45 mm thick joints. Neither different solution method nor finer meshing changed the sharp character of 45 mm joints curve. The explanation is in different reasons of the collapse. The internal strain energy is calculated as a product of stress and strain. Since the wall with 10 mm thick joints reaches almost the same loading as the wall with 45 mm thick joints, but smaller displacement, it also attains lower internal strain energy. Therefore, the wall with 10 mm joints fails due to exhausting its load-bearing capacity, which is quite gradual, whereas the wall with 45 mm thick joints collapses due to reaching its fracture energy and this is manifested by a sudden failure. What happens if the fracture energy is increased will be shown in Section 5.4.2.

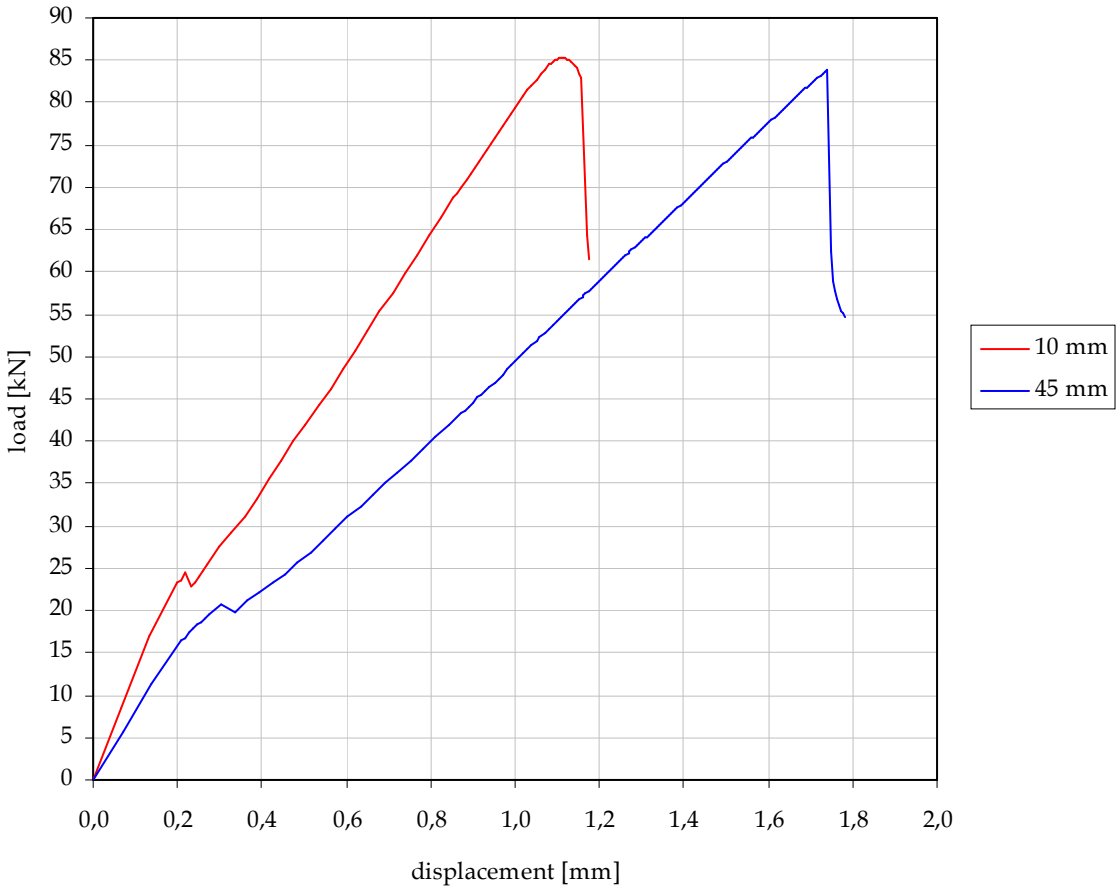

Fig. 5.11: Shear walls with 10 mm thick joints and with 45 mm thick joints

The difference in the behavior of the particular walls in the vicinity of the peak is well illustrated in Figures 5.12 and 5.13.

As you can see, the cracking is in the case of the wall with 10 mm thick joints very gradual. The state of the crack distribution 0,015 mm before peak is almost the same as in the peak itself and it necessary to go 0,06 mm beyond the peak to reach the cracking of a diagonal.

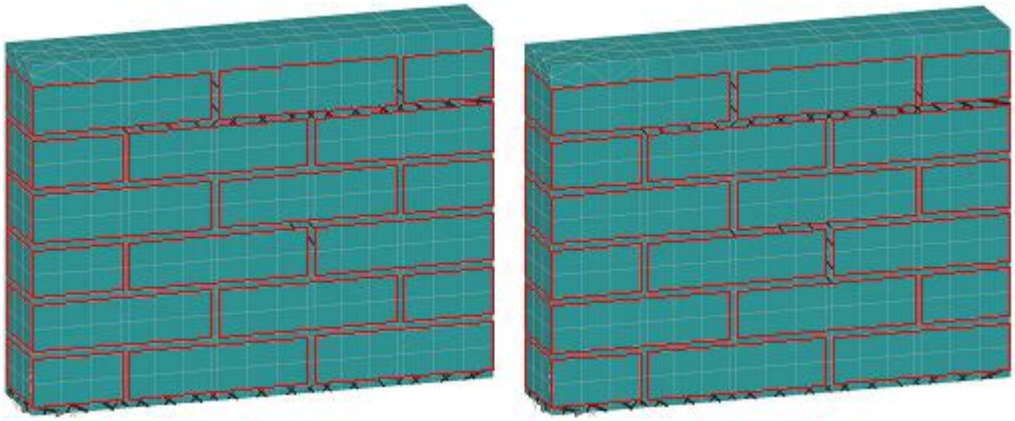

(a) 0,015 mm before peak *(b) peak*

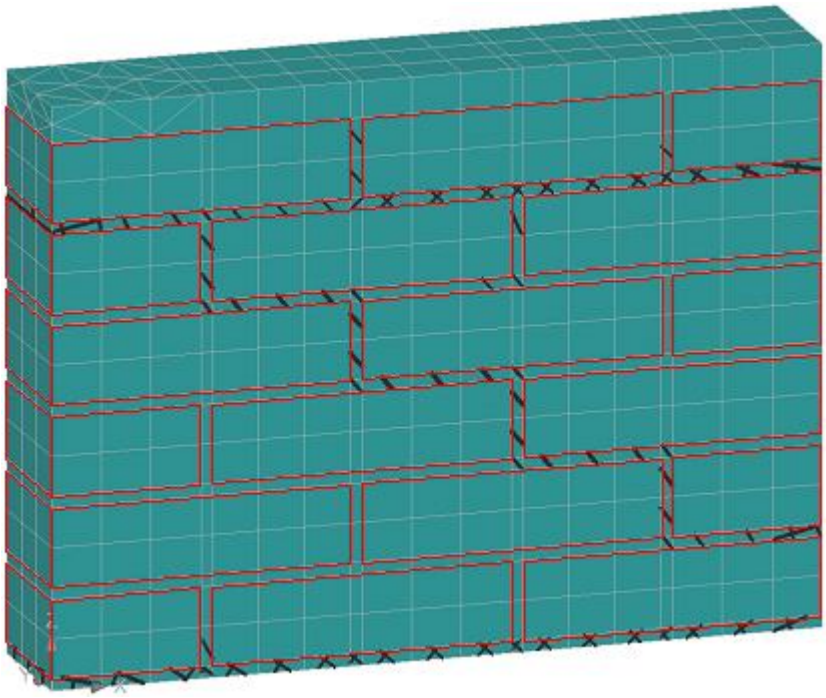

(c) 0,06 mm beyond peak

Fig. 5.12: Behavior of wall with 10 mm thick joints in vicinity of peak

On the contrary, in the case of 45 mm joints, a small change on the diagonal is visible even between 0,015 mm before peak and peak itself, and the diagonal

completely cracks 0,01 mm beyond peak only. The crack evolution is really fast beyond the peak.

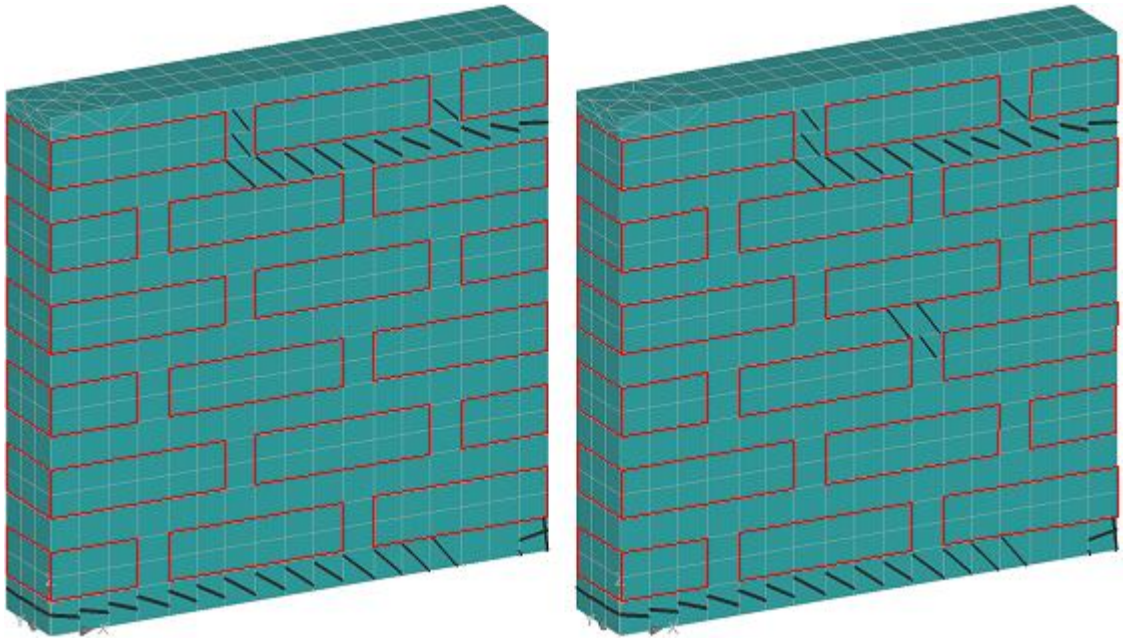

(a) 0,015 mm before peak *(b) peak*

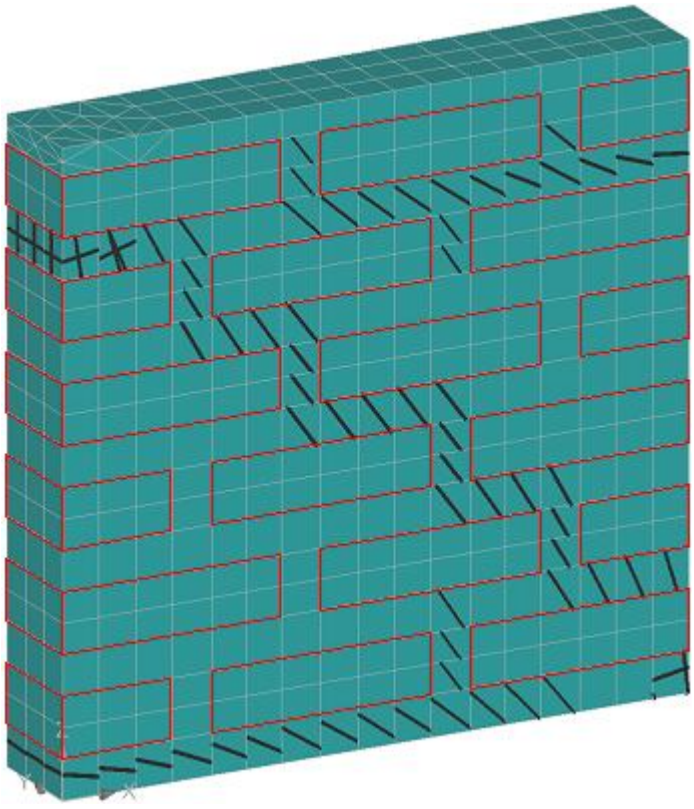

(c) 0,01 mm beyond peak

Fig. 5.13: Behavior of wall with 45 mm thick joints in vicinity of peak

5.3.2 Head Joints

An interesting idea is to observe the influence of head joints (the vertical ones) on load-bearing capacity of the wall. This strategy was inspired by Maheri et al. (2008) [29]. The authors of that paper noted that omitting the head joints even more

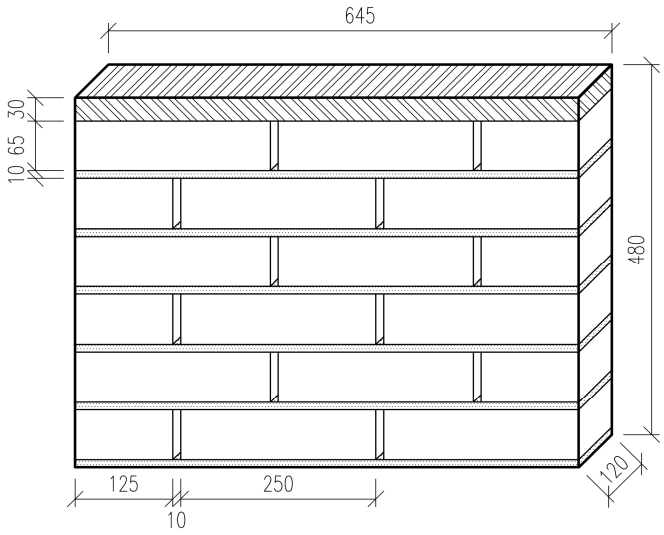

Fig. 5.14: Shear wall with 10 mm thick joints without head joints

decreases the stiffness of the wall. This strategy combined with thick joints could create a very compliant structure. Therefore, the wall with 10 mm thick joints without the head joints was modeled, see Figure 5.14, to compare the properties of

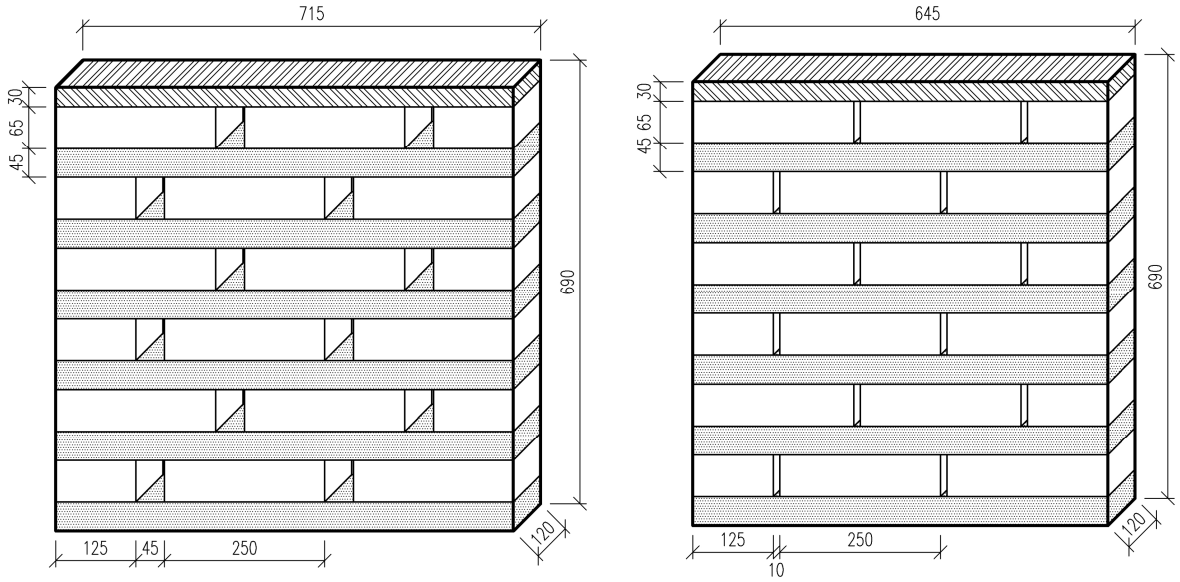

(a) without 45 mm thick head joints *(b) without 10 mm thick head joints*

Fig. 5.15: Shear walls with 45 mm thick joints without head joints

the standard walls with/without the head joints.

The wall with 45 mm thick joints without head joints was created as well. However, omission of 45 mm thick head joints looks very strange, as you can see in Figure 5.15 (a), and it probably would not be practical in-situ either. Therefore, a hybrid wall with 45 mm thick bed joints and only 10 mm thick head joints, which were omitted, was modeled. It is illustrated in Figure 5.15 (b).

The materials, bricks and loading procedure are the same as described in section 5.3. A comparison of the walls with 10 mm thick bed joints and with/without the head joints is in the Figure 5.16. Values of the peaks are shown in Table 5.6.

Table 5.6: Peak values for walls with 10 mm thick bed joints and with/without head joints

Head joints	Displacement [mm]	Load [kN]
yes	1,11	85,38
no	0,95	59,79

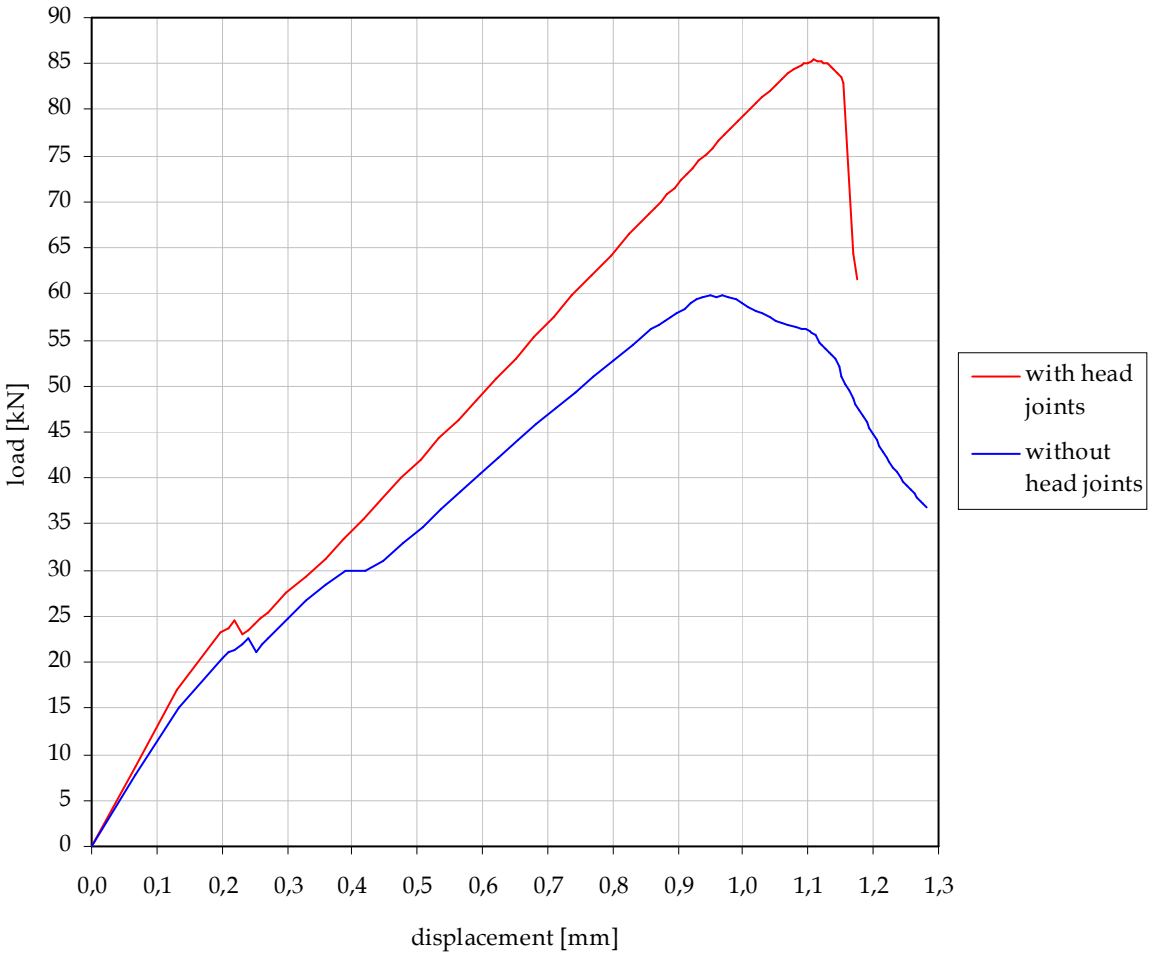

Fig. 5.16: Shear walls with 10 mm thick bed joints and with/without head joints

By mere glancing at the graph, we can say that omitting the head joints actually brought no benefits. The structure is more compliant and ductile, but the important properties, such limit deformation and load-bearing capacity, decreased significantly. The cracked wall just beyond the peak is in Figure 5.17.

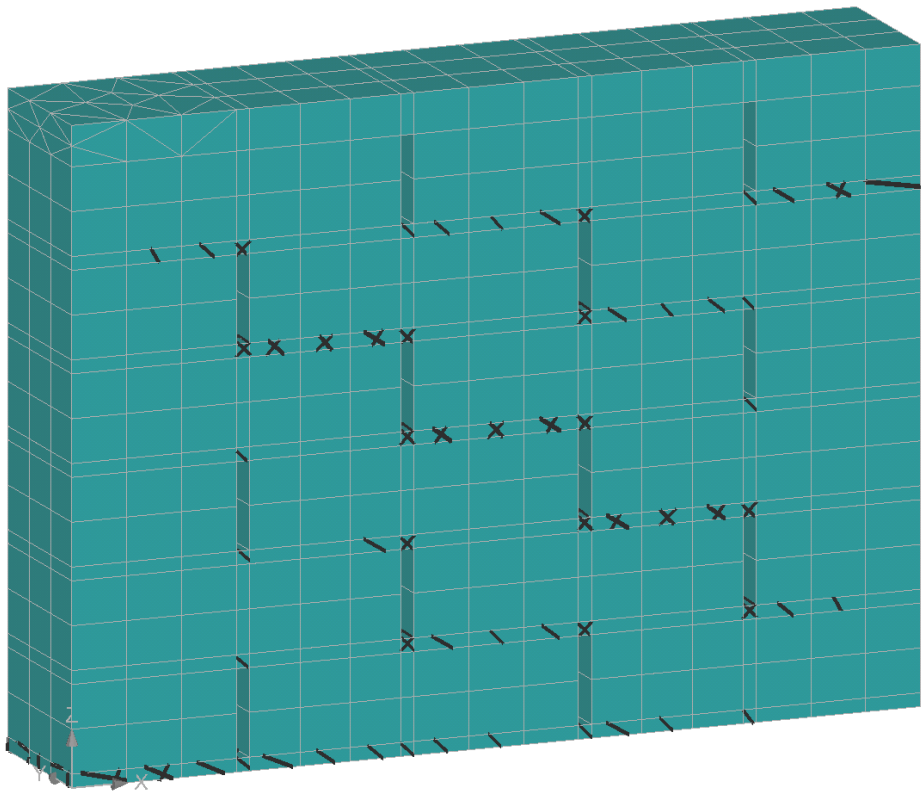

Fig. 5.17: Crack pattern of wall with 10 mm thick bed joints without head joints

Results of the analyses of the walls with 45 mm thick bed joints are depicted in Figure 5.18. As already mentioned, two types of the head joints (i.e. 10 mm and 45 mm) were omitted. In this case, the results of walls without the head joints are not worse so evidently. The coordinates of the peaks of the individual walls appear in Table 5.7. It is obvious that if we want to omit any head joints, then definitely

Table 5.7: Peak values for walls with 45 mm thick bed joints and with/without head joints

Head joints	Displacement [mm]	Load [kN]
yes	1,74	83,85
no - 10 mm	2,40	65,17
no - 45 mm	1,98	57,45

the thinner ones. The omission of the 45 mm thick head joints meant growth of limit displacement, but resistance of the structure decreased considerably. The wall without 10 mm thick head joints shows similar properties, but in a way that is more favorable, because limit displacement increased even more than in the case of omitted 45 mm joints, and the wall is also able to withstand higher load, but still lower than in the case of the full joints. The crack distribution of both cases is shown in Figure 5.19.

In summary, omitting the head joints in the case of the wall with thin joints has no positive effect. However, in the case of the wall with thick joints, the omission of the thin head joints can be helpful. If we need a structure that is more compliant and, at the same time, we know that load-bearing capacity of such a weakened structure is still high enough, then the wall with 45 mm thick bed joints and without 10 mm head joints is a wise choice.

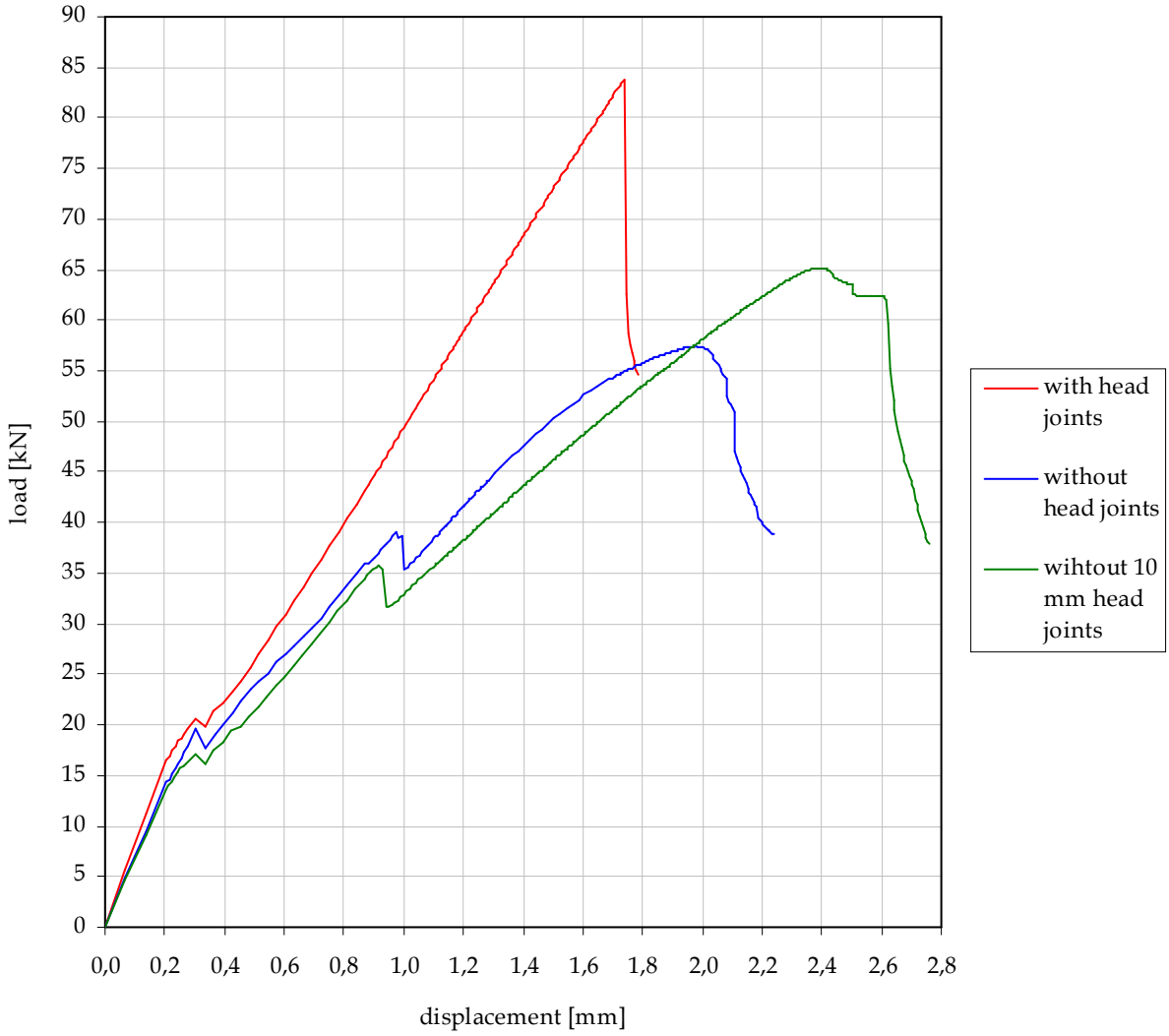

Fig. 5.18: Shear walls with 45 mm thick bed joints and with/without head joints

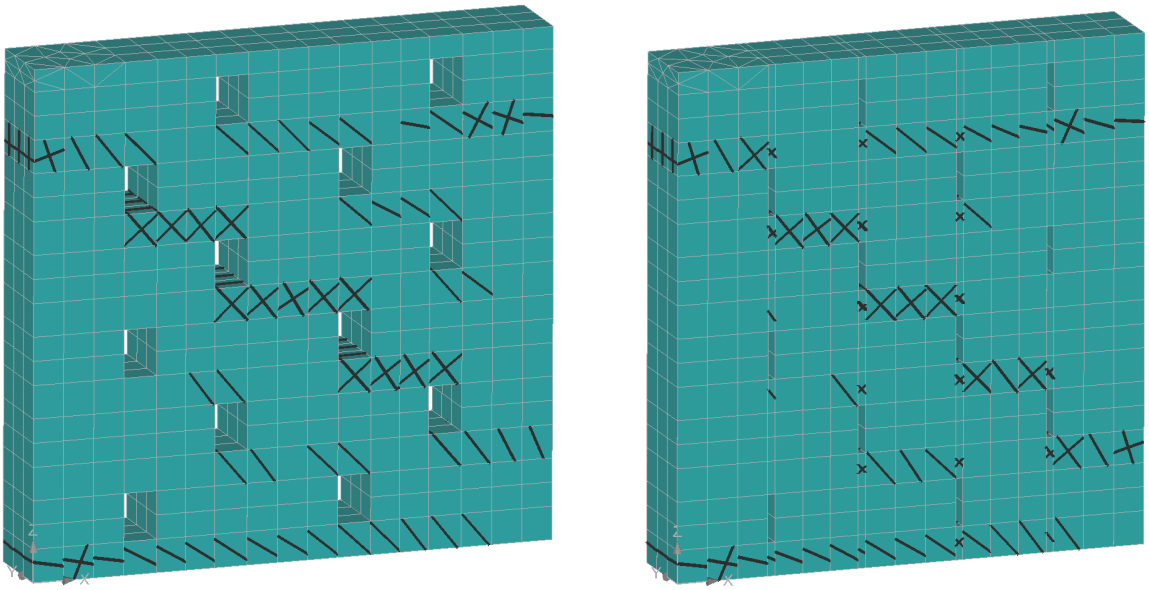

(a) without 45 mm thick head joints *(b) without 10 mm thick head joints*

Fig. 5.19: Crack pattern of wall with 45 mm thick bed joints without head joints

5.4 Influence of Material Properties

In this section, an impact of different material properties on behavior of the walls is investigated.

Now, the walls have always the same dimensions, i.e. all the walls have 45 mm thick joints and no joints are omitted, as shown in Figure 5.20, and it is not changed all through the section.

The same bricks with the same properties as in previous section are used, but properties of the cocciopesto mortar are changed from case to case, as described next.

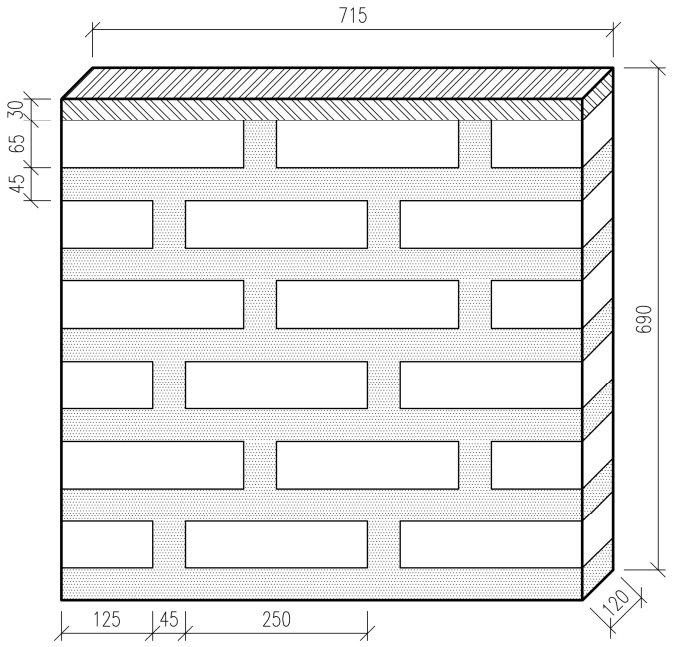

Fig. 5.20: Shear wall with 45 mm thick joints

5.4.1 Young's Modulus

Default value of the modulus is 2200 MPa. This value was being gradually lowered to 2000, 1800, 1600 and finally to 1400 MPa. To better see the trend of the response of the wall with different moduli, the value 3000 MPa was added.

Curves of all the analyses are plotted in Figure 5.21. Apparently, the shapes of the curves are absolutely the same. Just inclinations are different, but it is not surprising, if we take into account that the Young's modulus determines the angle between the horizontal axis and the elastic curve. However, also the peak values change. The summary of the peak coordinates, in dependence on the Young's modulus, is in the Table 5.8.

The tendency is clear. With decreasing elastic modulus, the limit displacement increases, while load-bearing capacity decreases. It can be interpreted by means of the internal strain energy again. The higher is the Young's modulus, the faster the

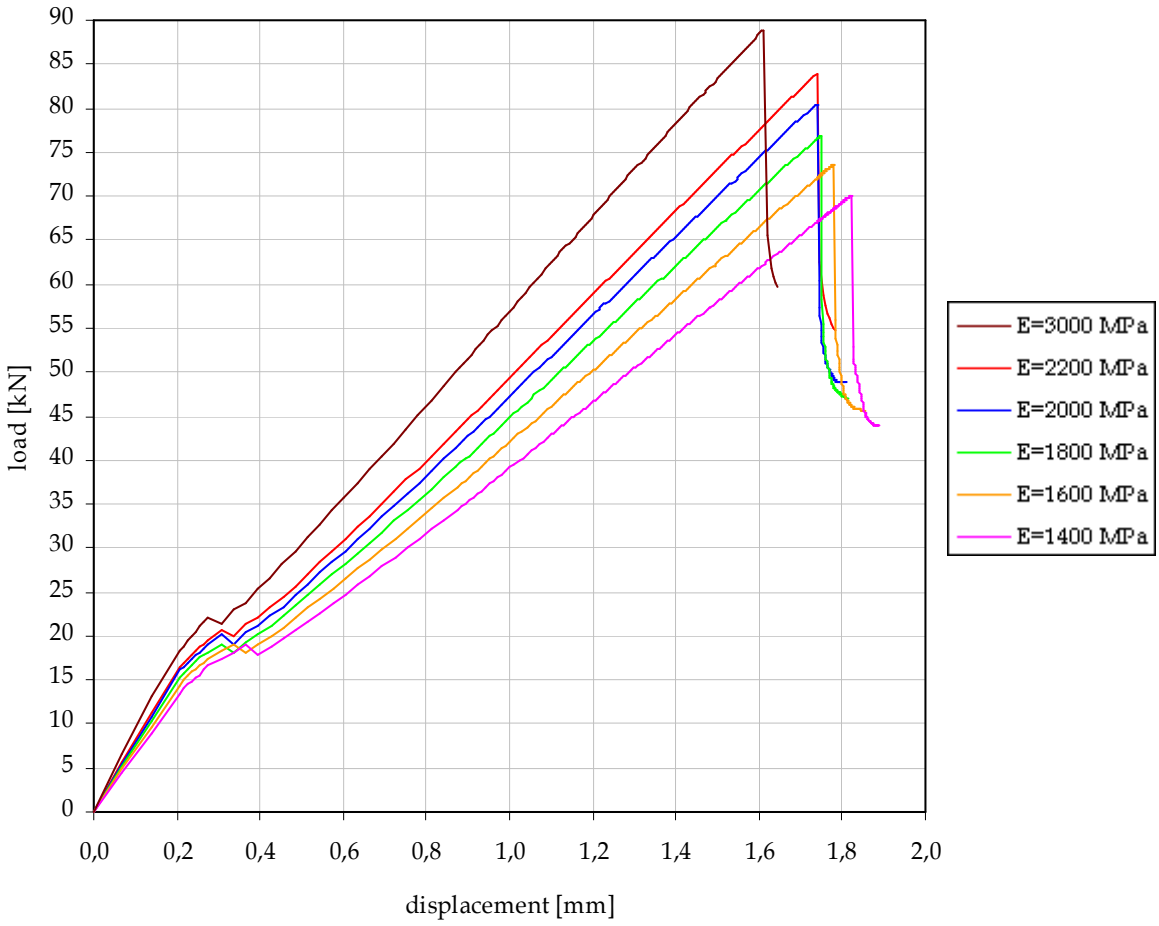

Fig. 5.21: Shear walls with different values of Young's modulus

curve reaches higher values of loading. If the product of stress and strain should be kept constant, the limit displacement must be inevitably lower.

Of course, there are small deviations not matching the explanation, especially in the case of the values of moduli 2200 MPa and 2000 MPa, where the maximum loads

Table 5.8: Summary of peak values for different Young's moduli

Young's modulus E [MPa]	Displacement [mm]	Load [kN]
3000	1,61	88,89
2200	1,74	83,85
2000	1,74	80,47
1800	1,75	76,86
1600	1,78	73,63
1400	1,82	70,05

differ, whereas the limit displacements are the same. Nevertheless, the difference of their load-displacement products is just 4%, which is not significant and can be caused by many irrelevant factors. Therefore, it is negligible.

Figures of the cracked walls are very similar for all moduli, therefore just one representative Figure 5.22 for E=2200 MPa is shown.

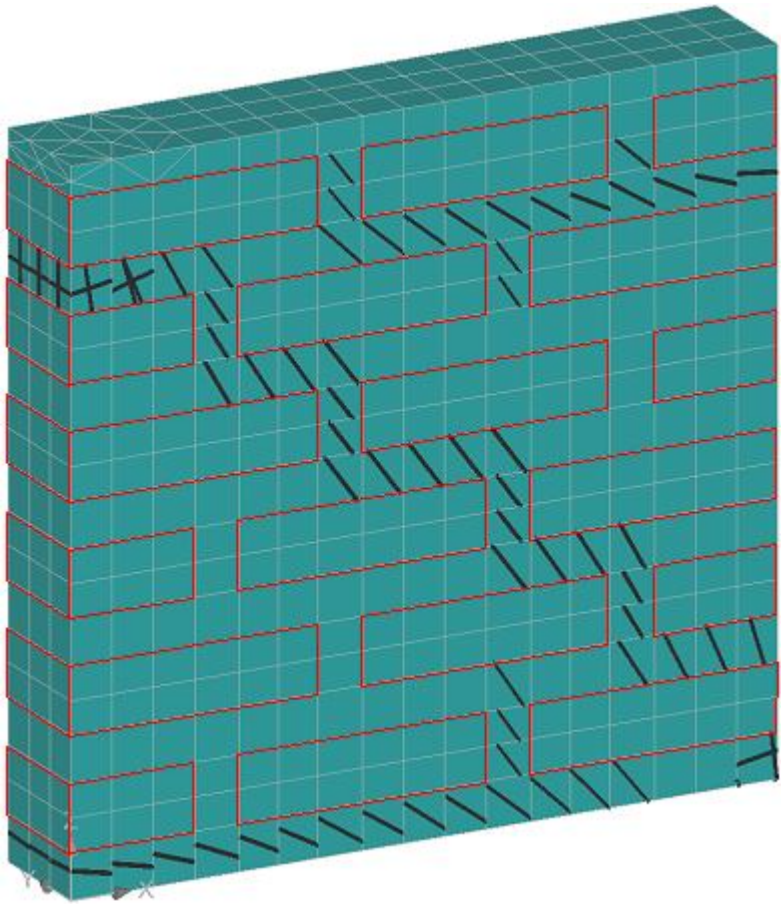

Fig. 5.22: Crack pattern of wall with 45 mm thick joints and Young's modulus 2200 MPa

5.4.2 Fracture Energy

It was discussed in Section 5.3.1 that the sharp peak of the wall with 45 mm thick joints is caused by reaching of the fracture energy, which did not allow the wall to exhaust its load-bearing capacity. On the contrary, peak of the wall with 10 mm thick joints was rounded, due to gradual cracking, because the strength was exceeded. This explanation can be now verified by changing values of the fracture energy.

Default value of the fracture energy is 19,55 Jm^{-2}. It was then increased 5 times and 10 times and also decreased 5 times and 10 times.

Graphs of the analyses are plotted in Figure 5.23. As expected, the shape of the peak really changed. When the fracture energy was increased, either 5 or 10 times, it became so high that the limit of a load-bearing capacity was reached sooner than the limit of fracture energy, causing a gradual cracking of the wall. The fact that the peak

stays sharp, if the fracture energy is either 5 or 10 times lowered, only confirms the idea of the different reasons of collapse.

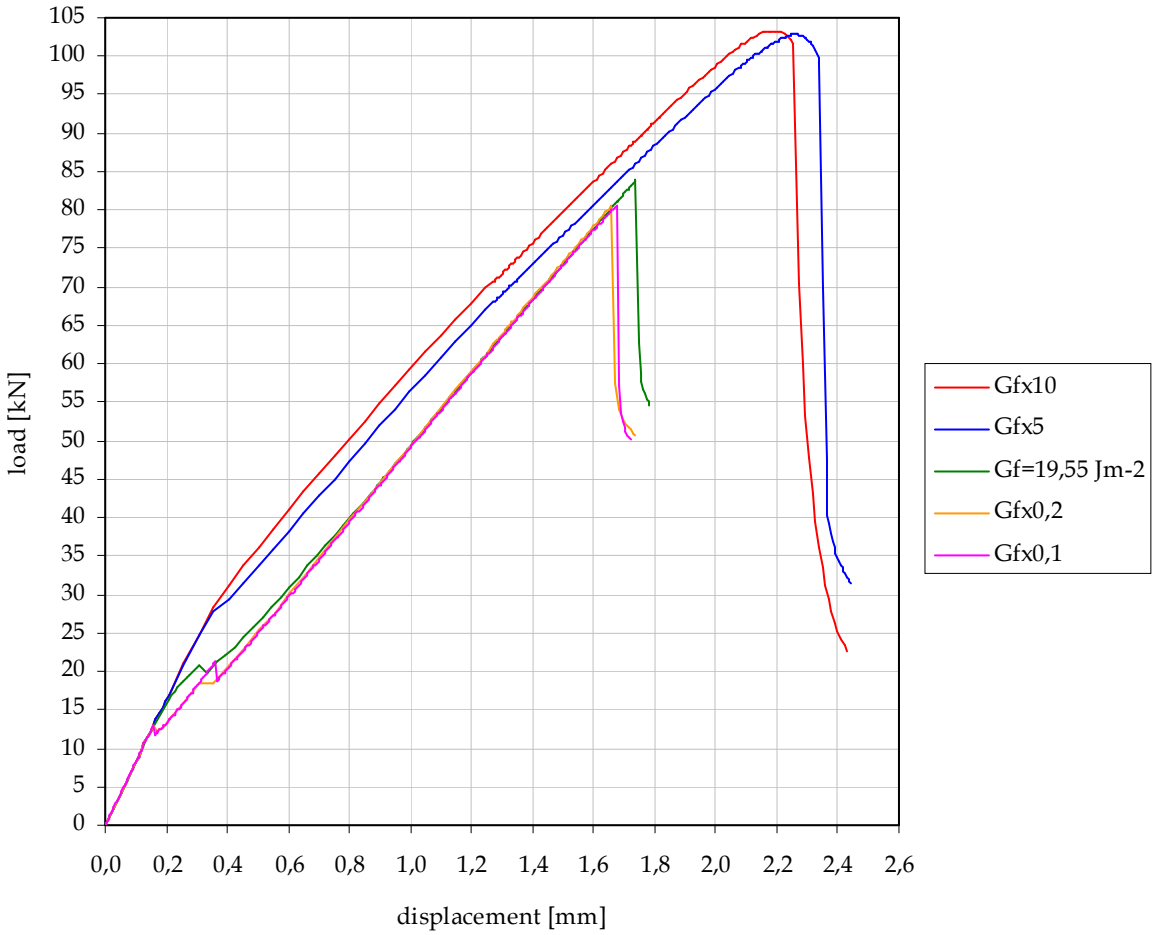

Fig. 5.23: Shear walls with different values of fracture energy

The values of the individual peaks are gathered in Table 5.9. Both the limit displacement and limit load increased quite significantly. It actually shows where the material strength limits of the structure are, if it is not limited by the fracture energy.

After first glance, it may seem strange that limit displacement of G_fx10 is lower than for G_fx5, but it can be easily explained. There is a break on the G_fx5 curve in an initial phase of loading, approximately at 28 kN. It is caused by first cracks, but the G_fx10 curve is smooth in this area. It is clear, because in the case of G_fx10, the energy necessary for first cracks was so high that it was not reached. As a result of this difference, the G_fx10 curve is, for the most of the time, higher than the G_fx5 curve. Nevertheless, if the areas below the graphs should be equal, than the value of the limit displacement of the G_fx10 curve must be lower.

If the value of the fracture energy is lowered, the curve develops in the same manner, as in the case of the default fracture energy, also the shape of the peak is still sharp, just the collapse comes sooner. Further lowering of the fracture energy plays a negligible role, as you can see from both graphs and table.

Table 5.9: Summary of peak values for different fracture energies

Fracture energy G_f [Jm^{-2}]	Displacement [mm]	Load [kN]
G_fx10	2,19	103,30
G_fx5	2,27	102,80
G_f=19,55	1,74	83,85
G_fx0,2	1,66	80,62
G_fx0,1	1,67	80,60

Crack patterns are relatively different for each value of the fracture energy. Therefore, there are depicted two representatives of extreme values, i.e. G_fx0,1 and G_fx10 in Figure 5.24. We can see that the cracks are really distributed differently. In the case of G_fx0,1 the diagonal is obviously decisive. Whereas in the case of G_fx10 the cracks are distributed more evenly meaning that the material is more utilized.

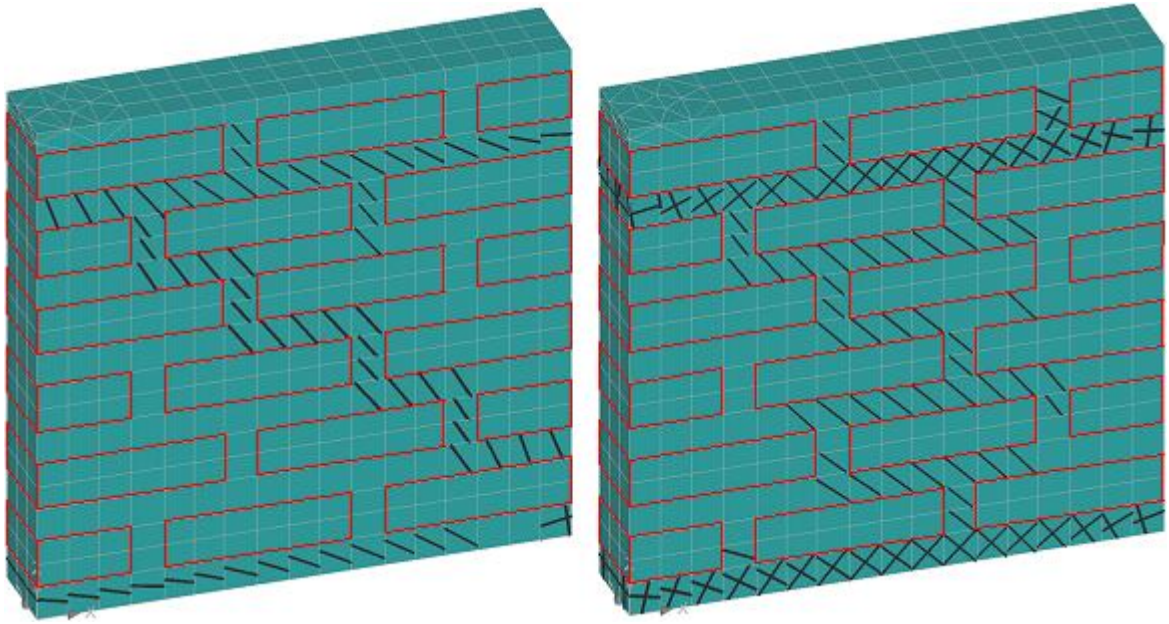

(a) fracture energy G_f x 0,1 *(b) fracture energy G_f x 10*

Fig. 5.24: Crack pattern of wall with 45 mm thick joints and different fracture energies

5.4.3 Tensile Strength

Since materials like concrete or mortar are known for their low tensile strengths, it is possible to expect that changes in the strength will have a certain effect on the overall structural behavior. The default value is 0,7 MPa. It was then increased to 0,9 and 1,1 MPa and also decreased to 0,5 and 0,3 MPa.

Results of the analyses are plotted in Figure 5.25. All the curves have very similar shape with the same inclination and only the peak values differ. However, we can see that the peak values change considerably, as the tensile strength changes. By increasing the default value about 0,4 MPa only, the peak moved higher and further, in the coordinate axes, than in any other case of material property or geometry change, and this is also similarly valid vice versa. If the default value is lowered about 0,4 MPa only, the limit properties of the wall are very unfavorable.

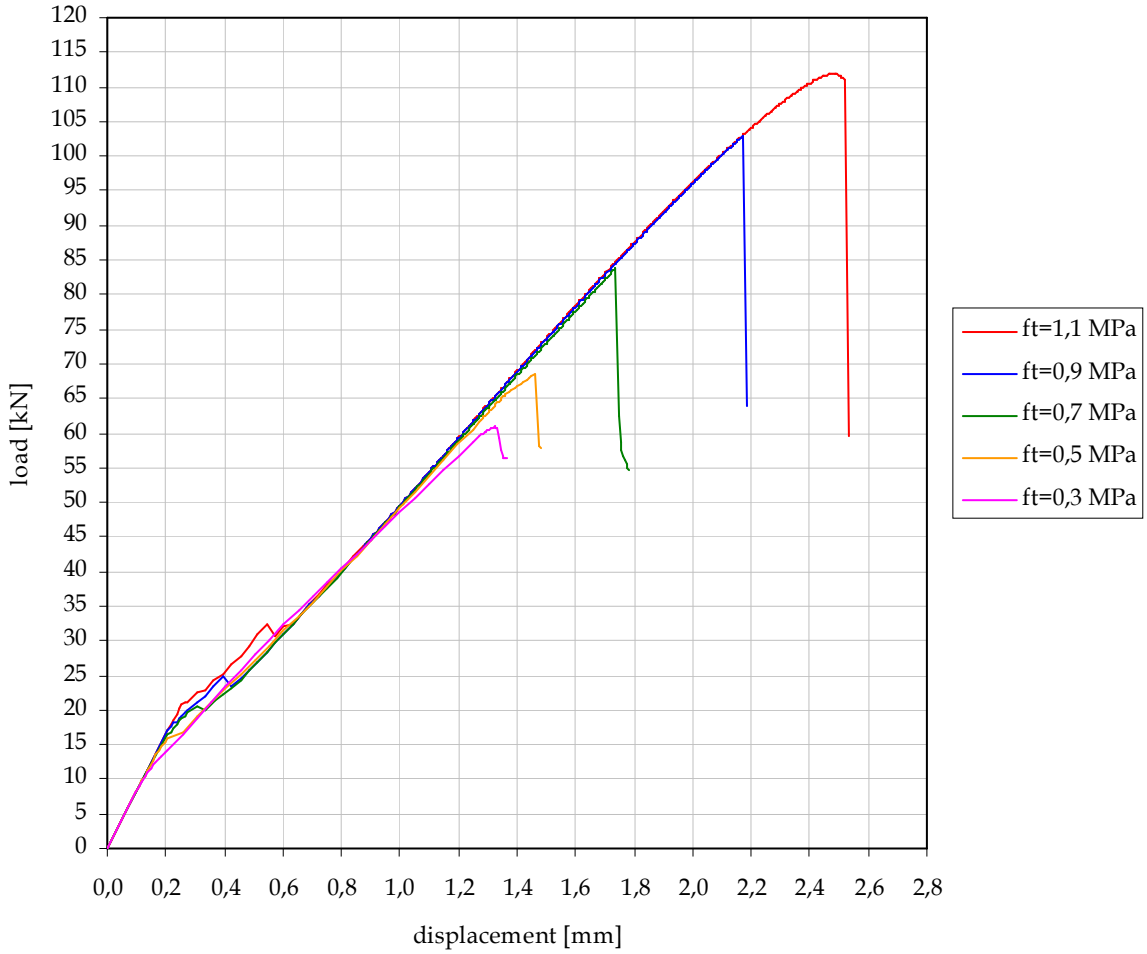

Fig. 5.25: Shear walls with different values of tensile strength

Table 5.10 illustrates the changes of the peak values by concrete numbers. From this, a conclusion can be drawn that the tensile strength influences the behavior very significantly.

Table 5.10: Summary of peak values for different tensile strengths

Tensile strength f_t [MPa]	Displacement [mm]	Load [kN]
1,1	2,49	111,90
0,9	2,17	102,90
0,7	1,74	83,85
0,5	1,46	68,48
0,3	1,32	60,90

Crack patterns also change together with the change of the tensile strength. In the case of a high tensile strength (i.e. 1,1 MPa), the collapse comes due to severe cracking of the two most exposed joints. As the tensile strength of the mortar is high, even a crack in a brick in the left top corner appears, as you can see in Figure 5.26 (a).

When a low value of the tensile strength (i.e. 0,3 MPa) is set, the wall shows many cracks spread through the joints, because even small tension is enough to initiate cracking. This is illustrated in Figure 5.26 (b).

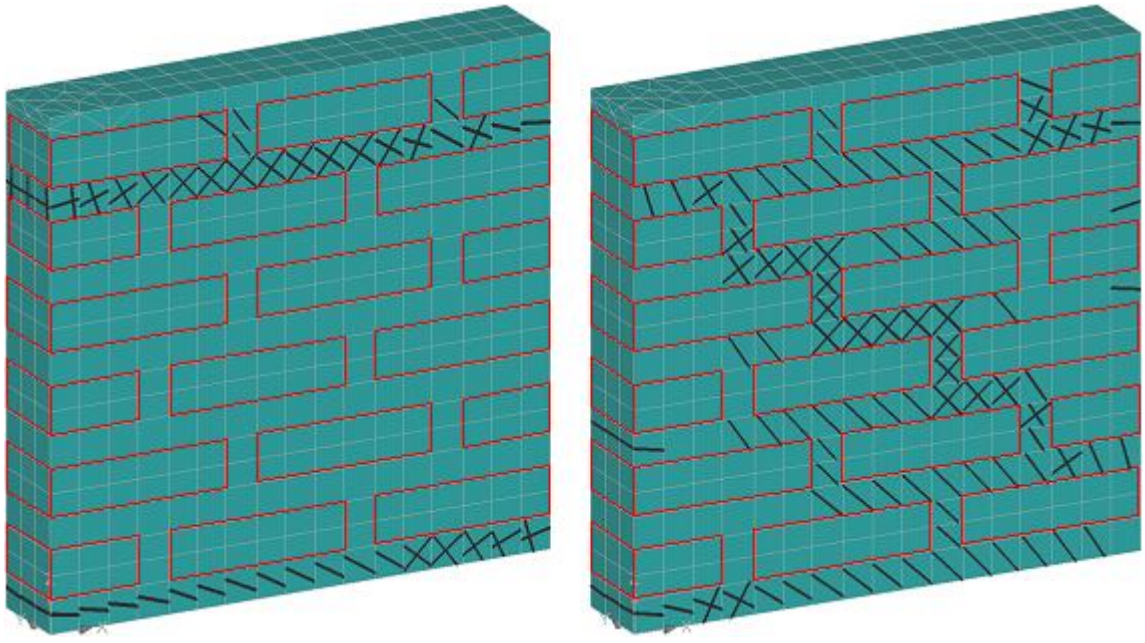

(a) tensile strength 1,1 MPa *(b) tensile strength 0,3 MPa*

Fig. 5.26: Crack pattern of wall with 45 mm thick joints and different tensile strengths

5.4.4 Compressive Strength

It is expected that the compressive strength will not influence the response of the wall in such extent as the tensile strength. The default compressive strength is 5 MPa, which was lowered to 3 MPa and then increased to 7, 9, and 11 MPa for next analyses.

Graphs of the analyses are depicted in Figure 5.27. The effect of the changed strengths is even lower than the expectations. We can see that all the curves, excepting 3 MPa, are extremely similar, almost identical.

This fact is just confirmed by Table 5.11, where the similarity of the peak values can be easily compared.

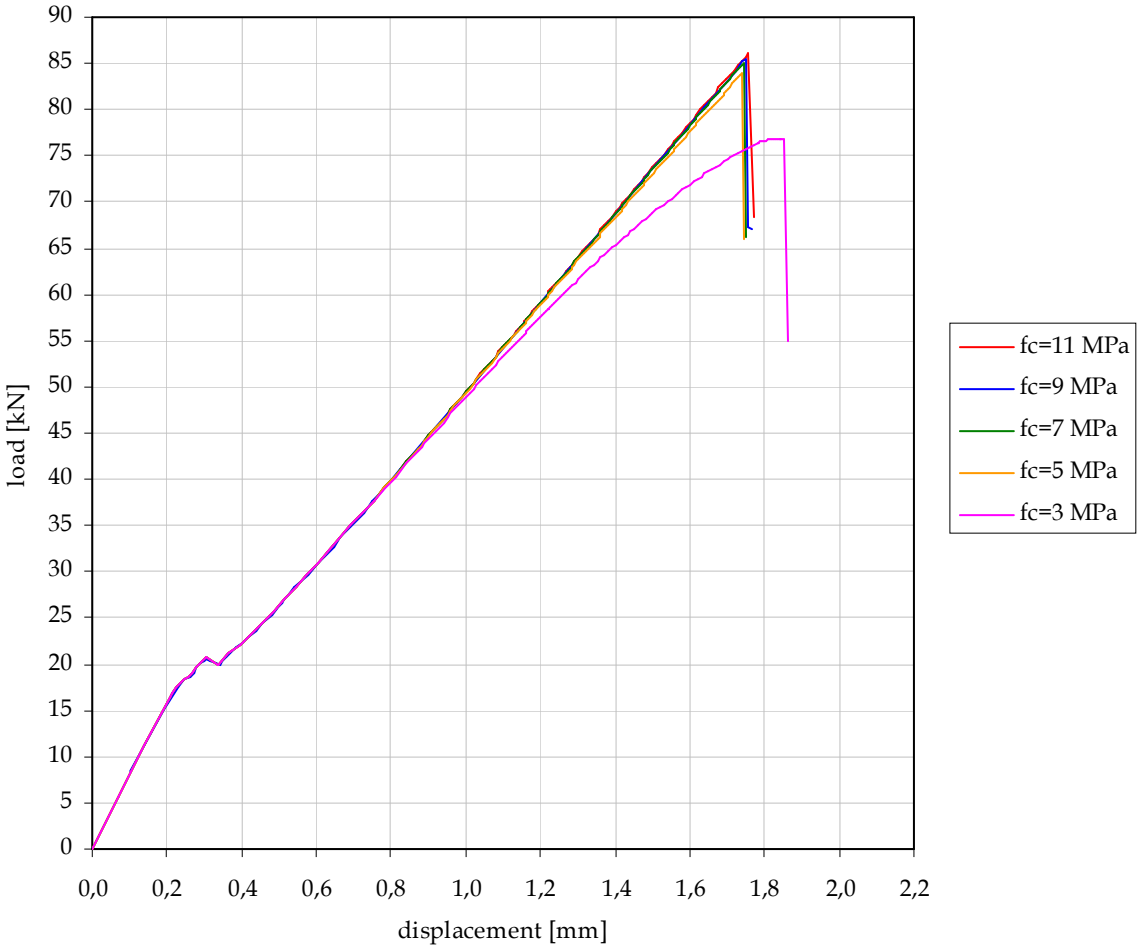

Fig. 5.27: Shear walls with different values of compressive strength

When the compressive strength is equal to 3 MPa, the mortar is weak in compression and therefore even a relatively low compression causes a crushing of the mortar. It makes the wall more compliant, which is illustrated by a slightly different shape of the corresponding curve.

Table 5.11: Summary of peak values for different compressive strengths

Tensile strength f_c [MPa]	Displacement [mm]	Load [kN]
11	1,76	86,10
9	1,75	85,50
7	1,74	85,02
5	1,74	83,85
3	1,70	76,85

Crack patterns are very similar for all values of the compressive strengths, therefore just one representative Figure 5.28 for f_c=5 MPa is shown.

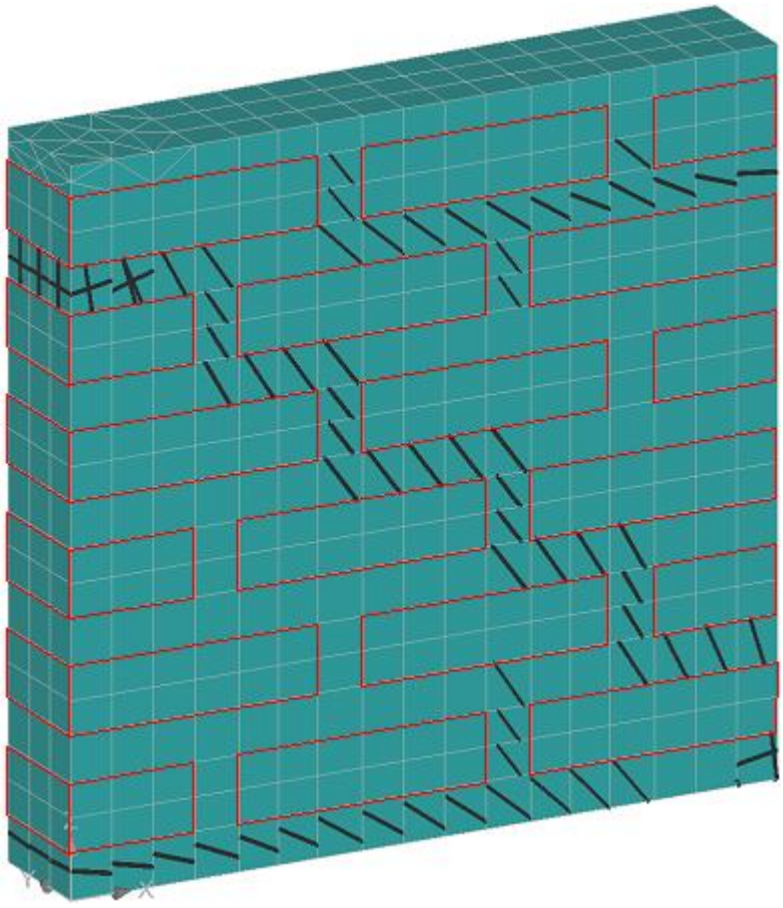

Fig. 5.28: Crack pattern of wall with 45 mm thick joints and compressive strength 5 MPa

6 Conclusion

It is clear now that the response of the masonry structures is, in most cases, strongly influenced by the geometry and material properties. By performing systematic numerical studies, the following geometrical parameters were found to be dominant:

- increase of the joint thickness from 10 mm to 45 mm rises the limit displacement significantly, while the load-bearing capacity changes negligibly and the collapse is more brittle
- omitting the head joints in the case of the wall with 10 mm thick joints decreases both the limit displacement and the load-bearing capacity
- omission of the 10 mm head joints in the wall with 45 mm thick bed joints increases the limit displacement and ductility, whereas the load-bearing capacity decreases

The output of the analyses with changing material properties is:

- with higher Young's modulus the load-bearing capacity is higher too, but the limit displacement decreases, nevertheless the difference in results is not substantial
- higher values of fracture energy considerably increases both the limit displacement and the load-bearing capacity, also the failure mode changes to more gradual
- the increased tensile strength results in higher limit displacement as well as the load-bearing capacity to a bigger extent than any other change of the material property
- difference in the compressive strength causes negligible changes in the limit displacement and the load-bearing capacity, the load-displacement curves are almost identical

The above-mentioned findings prove that the role of the thick joints in the behavior of the masonry structures is positive. More deformable but still strong structure is obtained, at least in the case of walls subjected to shear. The findings also reveal that omission of the head joints in wall with thin joints is useless. However, omitting the 10 mm head joints in the wall with 45 mm thick bed joints is reasonable if the deformability and ductility are more important than the load-bearing capacity. They also demonstrate that the fracture energy and tensile strength are worth changing in order to get better structural response.

For further analyses, it would be better to have available experimental data and a powerful computer enabling a use of finer meshes. Afterwards, it would be interesting to perform the fitting of the data obtained by the numerical analysis to the experimental ones by changing several material parameters at once.

References

[1] ZUCCHINI A., LOURENÇO P.B.: *A micro-mechanical homogenisation model for masonry: Application to shear walls*, International Journal of Solids and Structures, No. 46, 2009, pp. 871-886

[2] LOTFI H. R., SHING P. B.: *Interface model applied to fracture of masonry structures*, Journal of Structural Engineering, ASCE, vol. 120, no. 1, 1994, pp. 63-80

[3] GAMBAROTTA L., LAGOMARSINO S.: *Modeling the brick masonry shear wall response to seismic actions*, Proc. of Learning from Practice II: Damage Assessment for Design Decisions and Effectiveness of Techniques, L.A., 1997, pp. 47-62

[4] LOURENÇO P. B., ROTS. J. G.: *A multi-surface interface model for the analysis of masonry structures*, J. Engrg. Mech., ASCE, 123(7), 1997, pp. 660-668

[5] SENTHIVEL R., LOURENÇO P.B.: *Finite element modeling of deformation characteristics of historical stone masonry shear walls*, Engineering Structures, No. 31, 2009, pp. 1930-1943

[6] BRASILE S., CASCIARO R., FORMICA G. : *Multilevel approach for brick masonry walls – Part I: A numerical strategy for the nonlinear analysis*, Comput. Methods Appl. Mech. Engrg., 2007, pp. 4934-4951

[7] PALOMO A., VLANCO-VARELA M.T., MARTINEZ-RAMIREZ S., PUERTAS F., FORTES C.: *Historic Mortars: Characterization and Durability. New Tendencies for Research*

[8] MOROPOULOU A., BAKOLAS A., BISBIKOU K.: *Characterization of ancient, Byzantine and later historic mortars by thermal and X-ray diffraction techniques*, Thermochimica Acta, No. 269/270, 1995, pp. 779-995

[9] MOROPOULOU A., CAKMAK A.S., BISCONTIN G., BAKOLAS A., ZENDRI E.: *Advanced Byzantine cement based composites resisting earthquake stresses: the crushed brick / lime mortars of Justinian's Hagia Sophia*, Construction and Building Materials, No. 16, 2002, pp. 543-552

[10] SIDDALL R.: *Textures in Roman Lime Mortars using Polarising Light Microscopy*, http://www.ucl.ac.uk/~ucfbrxs/PLMlimes.html

[11] GIBSON P.: Pozzolans for Lime Mortars, http://www.buildingconservation.com/articles/pozzo/pozzo.htm

[12] BAKOLAS A., AGGELAKOPOULOU E., MOROPOULOU A.: *Evaluation of pozzolanic activity and physico-mechanical characteristics in ceramic powder-lime pastes*, Journal of thermal Analysis and Calorimetry, Vol. 92, 2008, No. 1, pp. 345-351

[13] BARONIO G., BINDA L., LOMBARDINI N.: *The role of brick pebbles and dust in conglomerates based on hydrated lime and crushed bricks*, Construction and Building Materials, Vol. 11, No. 1, 1997, pp. 33-40

[14] MOROPOULOU A., BAKOLAS A., BISBIKOU K.: *Investigation of the technology of historic mortars*, Journal of Cultural Heritage, No. 1, 2000, pp. 45-58

[15] NARASAIAH G. L.: *Finite Element Analysis*, BS Publications, 2008, pp. 26-92

[16] http://www.simtop.de/cgi-bin/rmcat?19990308_e

[17] http://solidmechanics.org/text/Chapter5_7/Chapter5_7.htm

[18] RAO S. S.: *The Finite Element Method in Engineering, fourth edition*, Elsevier Butterworth-Heinemann, 2005, pp. 83-84

[19] ROYLANCE D.: *Mechanical Properties of Materials*, 2008

[20] ŠEJNOHA J., ŠEJNOHA M., ZEMAN J., SÝKORA J., VOREL J.: *A mesoscopic study on historic masonry*, Structural Engineering & Mechanics, 30 (1), 2008, pp. 99-117

[21] ČERVENKA J., PAPANIKOLAOU V. K.: *Three dimensional combined fracture-plastic material model for concrete*, International Journal of Plasticity 24, 2008, pp. 2192-2220

[22] MENÉTREY P., WILLAM K. J.: *Triaxial failure criterion for concrete and its generalization,* ACI Structural Journal 92 (3), 1995, pp. 311–318

[23] JIRÁSEK M., ZEMAN J.: *Přetváření a porušování materiálů: dotvarování, plasticita, lom a poškození,* skripta ČVUT v Praze, 2008, pp. 83-102

[24] ČERVENKA V., JENDELE L., ČERVENKA J.: *ATENA Program Documentation, Part 1 – Theory*, 2005

[25] KABELE P.: *Nelineární analýza materiálů a konstrukcí*, přednášky, 2008

[26] BATHE K. J., CIMENTO A. P.: *Some practical procedures for the solution of nonlinear finite element equations*, Computer methods in applied mechanics and engineering 22, 1980, pp. 71-73

[27] NEŽERKA V.: *Report 1 (micromechanics)*, internal research report, Faculty of Civil Engineering, CTU in Prague, 2011

[28] BRENCICH A., CORRADI C., GAMBAROTTA L., MANTEGAZZA G., STERPI E.: *Compressive Strength of Solid Clay Brick Masonry under Eccentric Loading*, Department of Structural and Geotechnical Engineering, University of Genoa, Italy

[29] MAHERI M. R., NAJAFGHOLIPOUR M. A., RAJABI A. R.: *The influence of mortar head joints on the in-plane and out-of-plane seismic strength of brick masonry walls*, The 14th World Conference on Earthquake Engineering, Beijing, China, 2008